
Princeton Plasma Physics Laboratory

PPPL-

PPPL-



Prepared for the U.S. Department of Energy under Contract DE-AC02-09CH11466.

Princeton Plasma Physics Laboratory

Report Disclaimers

Full Legal Disclaimer

This report was prepared as an account of work sponsored by an agency of the United States Government. Neither the United States Government nor any agency thereof, nor any of their employees, nor any of their contractors, subcontractors or their employees, makes any warranty, express or implied, or assumes any legal liability or responsibility for the accuracy, completeness, or any third party's use or the results of such use of any information, apparatus, product, or process disclosed, or represents that its use would not infringe privately owned rights. Reference herein to any specific commercial product, process, or service by trade name, trademark, manufacturer, or otherwise, does not necessarily constitute or imply its endorsement, recommendation, or favoring by the United States Government or any agency thereof or its contractors or subcontractors. The views and opinions of authors expressed herein do not necessarily state or reflect those of the United States Government or any agency thereof.

Trademark Disclaimer

Reference herein to any specific commercial product, process, or service by trade name, trademark, manufacturer, or otherwise, does not necessarily constitute or imply its endorsement, recommendation, or favoring by the United States Government or any agency thereof or its contractors or subcontractors.

PPPL Report Availability

Princeton Plasma Physics Laboratory:

<http://www.pppl.gov/techreports.cfm>

Office of Scientific and Technical Information (OSTI):

<http://www.osti.gov/bridge>

Related Links:

[U.S. Department of Energy](#)

[Office of Scientific and Technical Information](#)

[Fusion Links](#)

Comparison of edge turbulence imaging at two different poloidal locations in the scrape-off layer of Alcator C-Mod

S.J. Zweben¹, J.L. Terry², M. Agostini³, W.M. Davis¹, A. Diallo¹, R.A. Ellis¹,
T. Golfopoulos², O. Grulke⁴, J.W. Hughes², B. LaBombard²,
M. Landreman², J.R. Myra⁵, D.C. Pace⁶, D.P. Stotler¹

¹ Princeton Plasma Physics Laboratory, Princeton, NJ 08540 USA

² Massachusetts Institute of Technology, Cambridge, MA 02139 USA

³ Consorzio RFX, Associazione EURATOM, I-35127, Padova, Italy

⁴ Max Planck Institute for Plasma Physics, EURATOM Association, D-17491 Greifswald, Germany

⁵ Lodestar Research Corporation, 2400 Central Ave., Boulder CO 80301, USA

⁶ General Atomics, PO Box 85608, San Diego, CA 92186-5608, USA

Abstract

This paper describes 2-D imaging measurements of plasma turbulence made in the scrape-off layer of the Alcator C-Mod tokamak simultaneously at two different poloidal locations, one near the outer midplane and the other near the divertor X-point region. These images were made with radial and poloidal resolution using two gas puff imaging (GPI) diagnostics, which were not directly connected along a B field line. The turbulence correlation structure has a significantly different tilt angle with respect to the local flux surfaces for the midplane and X-regions, and a slightly different ellipticity and size. The time-averaged turbulence velocities can be different in the midplane and X-regions, even within the same flux surface in the same shot, and in most cases the fluctuations in poloidal velocity in these two regions were not correlated. These structures are partially consistent with a magnetic flux tube mapping model, and the velocities are compared with various poloidal flow models.

I. Introduction

The general motivation for this paper is to better understand the plasma transport in the scrape off layer (SOL) of tokamaks. This is important since it partially determines the heat and particle deposition at the machine's divertor plates and first wall, and so will affect the engineering design of future tokamaks. The subject of plasma turbulence is also a challenging and fascinating topic in itself.

Turbulence in the edge of tokamaks is usually measured near the outer midplane where the edge turbulence level is large and diagnostic access is the easiest. However, since the theory and modeling of tokamak edge turbulence can now be done in 3-D geometry, including the X-point and divertor regions, it is interesting to try to validate such theory with 3-D measurements of the structure and motion of edge turbulence.

The present paper compares gas puff imaging (GPI) measurements made of edge turbulence at the outer midplane and X-point regions of Alcator C-Mod, as illustrated in Fig. 1. These measurements were made simultaneously with 2-D radial vs. poloidal resolution in both regions, although these two regions were *not* directly connected along a single magnetic field line due to diagnostic location constraints. The results were mainly obtained for the scrape-off layer (SOL) region outside the separatrix using standard C-Mod lower-single-null diverted discharges. For this paper the experimental results are compared only with simple theoretical models, since 3-D turbulence simulations of these discharges are not yet available.

The 3-D structure of SOL turbulence in tokamaks has been measured to a limited extent, as reviewed previously [1,2]. In general, edge density and electrostatic potential fluctuations tend to have a long correlation length along the magnetic field lines (i.e. many meters), as seen for example in JET [3], C-Mod [4], and NSTX [5]. This is due to the rapid electron motion along the magnetic field B , which equilibrates the potential at the electron thermal or Alfvén speed. The turbulence structure perpendicular to B is always much smaller (i.e. centimeter-scale), often forming spatially isolated and intermittent structures in the SOL known as blobs. Thus the 3-D structure of SOL turbulence generally consists of filaments aligned along B with small-scale structures perpendicular to B . However, the parallel correlation along B is not perfect, and some parallel variation is expected theoretically [6,7], for example, when the timescale for turbulent perpendicular $E \times B$ drifts is comparable to the parallel electron transit time, or due to variations in the magnetic structure, plasma parameters, or fluid velocities along B . Thus there may be significant poloidal variation in the structure of SOL turbulence.

Direct measurements of the poloidal variations of tokamak SOL turbulence were also reviewed in [1,2]. The clearest poloidal variation observed so far for diverted tokamaks is a large ($\times 10$) reduction in the turbulence level at the inner midplane (small major radius) compared with the outer midplane (large major radius), e.g. in Alcator C-Mod [8]. This is expected due to the difference in the interchange drive (“ballooning”), although no quantitative comparisons with theory have yet been made. Several measurements of turbulence have also been made using Langmuir probes in tokamak

divertor regions. A higher relative level of ion saturation current fluctuations was observed at the outer divertor target plates compared to the inner target in JET, with the highest level in the private flux region [9]. A vertically scanning probe in the DIII-D divertor showed large relative fluctuation levels ($\sim 10\text{-}100\%$) in potential (normalized to the electron temperature T_e) in the SOL and private flux region [10]. In MAST, the intermittency was high at the outboard (low field) divertor target plates, but low or absent around the X-point and high-field target plates [11]. In NSTX the turbulence at the divertor plate surfaces was measured using LiI line emission and showed an interesting pattern of toroidal vs. radial filamentation, which was correlated by field-line mapping to the midplane blob structures seen by GPI [5].

Initial GPI measurements of edge turbulence near the lower X-point region of C-Mod [12] showed unusually elongated 2-D turbulence structures compared with the nearly isotropic structures normally seen at the outer midplane [8]. This X-region structure was interpreted in terms of a magnetic flux tube model in which an assumed circular blob at the outer midplane was mapped along a flux tube to the GPI view at the X-region. The present paper uses the same X-region GPI view, but now directly compares the X-region and outer midplane turbulence measured at the same time (but not along the same field line), and also uses a wider C-Mod database and an improved GPI diagnostic. The present paper also compares the turbulence flow velocity at the outer midplane and X-point regions using these same two GPI views. This was motivated in part by recent measurements of zonal flows (i.e. GAMs), which showed a long-range correlation between edge velocity fluctuations at very different toroidal/poloidal locations [13-15]. The edge turbulence velocity in C-Mod was previously measured using GPI in the outer midplane region [16,17] but not in both regions simultaneously.

Recent Langmuir probe measurements of turbulent transport in the SOL of C-Mod have shown that the fluctuation-induced radial particle flux on the high field side midplane location much lower than at the low-field side midplane [18]. Also in C-Mod, a high correlation was recently measured between the turbulence at the outer midplane seen with GPI and Langmuir probe measurements near the X-point region which mapped magnetically to the region viewed by the GPI, and similarly between the outer midplane region that mapped magnetically to Langmuir probes in the outer divertor target plates [19].

In other tokamak devices, the most closely related recent work was done at Tore Supra, where the relationship between the turbulence structure, velocity, magnetic and electric field shear was analyzed for the SOL [20]. Turbulence measurements by probes at the top of ToreSupra were consistent with a model in which the turbulence was transported across the separatrix near the outer midplane, and propagated along B field lines to the top. Recent results from a dual GPI diagnostic on the EAST tokamak have also shown that the SOL turbulence structure and velocity were different $\pm 50^\circ$ above and below the outer midplane [20,21].

The outline of this paper is as follows: Sec. II describes some theoretical background relevant for this experiment, Sec. III describes the GPI diagnostic and data

analysis procedures, Sec. IV describes the experimental results, and Sec. V contains the discussion and conclusions.

II. Theoretical background

The basic theoretical issues relevant to this experiment concern the 3-D structure and motion of turbulence in the SOL of a diverted tokamak. In this paper ‘turbulence’ refers to density/electric field fluctuations and not to turbulent magnetic field fluctuations, which are usually small in the SOL (except perhaps during ELMs) and were not measured in this experiment.

Because of the rapid electron motion along B, the structure of the electrostatic potential is generally observed to have a parallel wavelength much longer than the perpendicular wavelength, but it is not clear whether the 3-D structure is flute-like (with $k_{\parallel}=0$) or drift-ballooning-like ($k_{\parallel}\sim 1/qR$), or whether some other scales may be involved. However, analytic calculations of tokamak geometry showed that the shape of a magnetic flux tube changes significantly as a function of poloidal angle in the SOL due to magnetic shear and flux expansion [22], which suggests that the turbulence structure should vary with poloidal angle.

An illustration of this magnetic flux tube variation is shown in Fig. 1 for a typical discharge in this experiment. The black filled shapes in the plot at the left shows how a 1 cm diameter circular flux tube started at 1 cm outside the separatrix at the outer midplane is distorted in shape and tilted as a function of the poloidal angle. By the time this flux tube reaches the X-region GPI view it is elongated by a factor of ~ 3 due to the flux expansion between these two regions, since the innermost and outermost radii of the flux tube remain the same in flux surface coordinates. Since the area of a flux tube depends inversely on B it decreases by a factor of ~ 0.8 from the outer midplane to the X-region view, and so the minimum width of the flux decreases by somewhat more than a factor of 3. The tilt angle of these flux tubes depends on the local magnetic shear near these flux surfaces, which depends on the plasma shape. The ellipticity and tilt of these flux tubes varies slowly over the X-region field of view, as shown in the map of X-region flux tubes at the lower right, all of which were mapped from 1 cm diameter circles at the outer midplane.

The radial and poloidal motion of isolated plasma blob-filaments in the SOL was calculated to depend on the poloidal location of the filament [23], which was assumed to extend only part of its length along the field line length in the SOL. The motion of the blob-filament was also shown to depend on its degree of connection with the divertor plate, which affects the electrostatic potential in the filament. The local acceleration acting on a segment of an ideal blob-filament is in the $-\nabla B$ direction [23]. These filaments can become disconnected from the divertor plate due to the narrowness of flux tubes near the X-point, or by a high electrical resistivity in the SOL [6]. The dynamics of blob-filaments can also be modified by drift wave formation in the SOL [7,24], and can be significantly affected by the parallel dynamics [6,25].

The effects of electric fields and electric field shear on the motion and structure of blobs has been addressed in model simulation studies. In a homogeneous background plasma, blobs convect with the local $\mathbf{E} \times \mathbf{B}$ drift velocity. If the $\mathbf{E} \times \mathbf{B}$ velocity is sheared, it will shear and possibly tear apart the blob structure [26]. The motion of the centroid of a blob is also affected by a velocity shear layer which can act to accelerate or decelerate it depending on the relative signs of vorticity of the shear layer and the blob [27]. Inhomogeneities in the background plasma modify both the blob motion and structure [27,28]. Finally, in the presence of toroidal rotation the blob-filaments, which have a density approximately constant along helical field lines, can acquire apparent poloidal motion when viewed at a fixed toroidal angle (the “barber pole” effect).

Several linear stability calculations have been done for 3-D tokamak geometry which show a variety of unstable ballooning modes and drift waves in the SOL. In the fluid limit the SOL stability depends on dimensionless parameters such as R/L_n , β , the parallel resistivity, the magnetic shear, and the assumed flux surface geometry and boundary conditions. The latter have varied from a realistically shaped diverted model with sheath boundary conditions [29] to a simplified circular limited model [30]. Not yet included in these models are kinetic effects, sheath instability effects, zonal flows, or atomic physics, which all could play a role in the SOL linear stability. Since the linear growth phase lasts only a fraction of a millisecond, and since experiments have shown that the SOL is normally turbulent, linear stability calculations are not considered to be relevant for comparison with experiments.

The nonlinear theory of edge turbulence is complicated [31]. Several numerical models have been developed using simplified 2-D geometry, but only a few models have tried to include the full 3-D geometry needed to understand the poloidal dependence of the turbulence. The 3-D edge turbulence was modeled in the BOUT fluid code, and initial comparisons were made with the structure of the turbulence in the C-Mod midplane [32] and X-point region [12]. The 3-D GEM-R gyrofluid code was compared with the midplane C-Mod GPI data [33], but not with C-Mod X-region data. SOL turbulence was modeled with the GBS code in a simplified toroidal geometry, and initial comparisons were made with TORPEX measurements [34]. Recently the BOUT code was used to calculate the edge and SOL turbulence in DIII-D, and the results appeared to agree well with midplane probe and BES measurements of turbulence [35].

Although plasma dynamics in the SOL are turbulent, it is nonetheless useful to consider what mean flows would be expected in the limit of a quiescent SOL. As discussed in the following section, the GPI cameras are oriented to look approximately parallel to \mathbf{B} , and so motion in the camera image should be associated with cross-field drifts rather than parallel motion. For these experiments in Alcator C-Mod, the toroidal field is clockwise when viewed from above, and so the ∇B drift, curvature drift, and ion diamagnetic drift directions are all downward in this experiment. To determine the $\mathbf{E} \times \mathbf{B}$ drift direction in Ohmically-heated plasmas, consider that the mean electric field in the SOL should point outward [36], which may be understood as follows. The potential on an open field line should be approximately given by the sheath potential $\Phi(r) \approx 3T(r)/e$, where T is the temperature near the divertor plate. As T decreases as

one moves outward from the separatrix, Φ decreases with it, giving an outward \mathbf{E} . The mean $\mathbf{E} \times \mathbf{B}$ flow in the Alcator C-Mod SOL should then be downward, yielding a total perpendicular flow that is also downward. Probe measurements confirm that \mathbf{E} in the Alcator C-Mod SOL is indeed consistently outward in both Ohmic L-mode and Ohmic H-mode, scaling roughly as T_e/e [37]. Fourier analysis of GPI images from Ohmic plasmas are also consistent with an outward E_r in the far-SOL with a magnitude roughly $-3dT_e/dr$ [17].

Consider next how the perpendicular flow may be expected to vary poloidally. We may expect the potential Φ , the pressure p , and the density n to be nearly constant on field lines between the two observation regions [38]. The magnitude of the perpendicular flow velocity is then the sum of the $\mathbf{E} \times \mathbf{B}$ and ion diamagnetic drift velocities $\left| B^{-2} \mathbf{B} \times \nabla \Phi + (neB^2)^{-1} \mathbf{B} \times \nabla p \right| = \omega |\nabla \psi| / B$ where $2\pi\psi$ is the magnetic flux and $\omega = d\Phi/d\psi + (ne)^{-1} dp/d\psi$ is nearly constant. Notice $|\nabla \psi| = 1/(\text{distance between } \psi \text{ contours})$, so $|\nabla \psi|$ is slightly larger at the midplane, while B is slightly smaller at the midplane. Thus, flows at the midplane location would be expected to be slightly larger than at the X-point location.

To the slight extent that the GPI cameras are not pointed perfectly parallel to \mathbf{B} , the measured flow may contain some contribution from the parallel flow. Flow along \mathbf{B} may appear on the cameras as either toward or away from the X-point depending on whether the pitch of the camera view is greater or less than the pitch of the field. Average parallel flow arises in the edge due to several factors, including Pfirsch-Schlüter effects [18], collisional (neoclassical) flow [39], and sources and sinks [36]. More detailed discussion of the relationship between this theory and the present experimental results is given in Sec. V.

III. GPI diagnostic and data analysis

This section describes the GPI diagnostic and data analysis used for this experiment. Sections Sec. III.A and B describe the hardware, Secs. III.C and D describe the diagnostic operation and database, and Secs. III.E and F describe the data analysis. Some of the limitations and uncertainties in the diagnostic and data analysis are described in Sec. G.

A. GPI overview and geometry

The gas puff imaging diagnostic has been used previously on Alcator C-Mod [8,12,16], NSTX [40], RFX-Mod [41], Gamma-10 [42], Heliotron J [43], TEXTOR [44], and EAST [20,21]. A localized neutral gas puff of D_2 or He is introduced near the vessel wall and viewed along the direction of the local magnetic field line using a fast camera. The neutral atom light emission in D_α (651 nm) or He I (587 nm) is resolved in the 2-D

radial vs. poloidal (i.e. binormal) plane on a spatial scale of a few millimeters and a timescale of a few microseconds. This light emission is limited to the region where $T_e \sim 10\text{-}100$ eV where these atoms are neutral, so the GPI can see only the edge and scrape-off layer (SOL) region of most tokamaks.

Since the neutral light emission is proportional to the local electron excitation, the space-time fluctuations of the light emission are interpreted in terms of the local electron density/temperature fluctuations. The space and time correlation functions are largely independent of the non-linearity between the underlying plasma density and/or temperature fluctuations and the neutral light emission [40,45]. The time-averaged 2-D profiles of neutral line emission have been successfully compared with calculations based on the measured edge temperature and density profiles and the neutral and atomic physics in the DEGAS 2 simulation, both for He in C-Mod [46] and D in NSTX [47]. The time response of the HeI line to fluctuations should be ≤ 1 μs for SOL plasmas [45].

Figure 1 shows a cross-section of an Alcator C-Mod plasma in the (R,z) plane along with the location of the two GPI viewing regions and sample magnetic flux surfaces. The plasmas have major radius of $R=67$ cm, a minor radius of $a=23$ cm, and a standard lower single-null divertor shape with an elongation of typically $\kappa=1.6$. The “midplane” GPI camera view is centered 3 cm below the outboard midplane, and the “X-region” GPI camera view is centered 30 cm below the midplane near (but not overlapping with) the divertor X-point. Both viewing regions are approximately square and extend ~ 5.9 cm radially and ~ 5.9 cm poloidally, covering the separatrix (solid line) and flux surfaces up to about $\rho=2$ cm outside the separatrix (dashed lines), where ρ is the radial distance outside the separatrix measured at the outer midplane. Note that the actual GPI optical sightlines are aligned along the local direction of the total magnetic field at these two locations (see Sec. III.B), so the regions shown in Fig. 1 are the projections of these views in the (R,z) plane.

The black circle shown at the outer the midplane in Fig. 1 is the cross-section of an assumed circular magnetic flux tube at $\rho=1$ cm outside the separatrix, and the other black shapes show how this flux tube is elongated and tilted as it follows the magnetic field line to different poloidal locations. These shapes show the intersection of flux tubes with planes of constant toroidal angle, which are very similar to the cross-sections perpendicular to B . Flux tubes with circular cross-sections at the outboard midplane transform into tilted elongated fingers at the poloidal location of the X-region view, with elongations of about a factor of 3.. This flux tube distortion occurs both above and below the midplane, so does not require the presence of an X-point. Similar looking flux tubes are obtained over all radii in the SOL of C-Mod (see Fig. 1 and [12]), and a similar-looking flux-tube distortion was calculated for the circular limited Tore Supra [20]. A 3-D visualization of the magnetic flux tube between these two poloidal locations is also shown at the upper right in Fig. 1.

Due to internal vessel constraints, these two GPI views were *not* designed so as to view the same magnetic field line in the SOL. Thus the comparisons between the midplane and X-region turbulence are not based on direct cross-correlations between

them, but on statistical differences in the turbulence structure and velocity between them. The specific location of these two views with respect to magnetic field line mappings is discussed in the Appendix.

B. GPI diagnostic hardware

The optical hardware for the midplane GPI view is the same as described previously [16]. An in-vessel telescope was mounted on the outer wall and pointed at the center of the midplane view of Fig. 1 in the local B field direction, which was 11° below horizontal, as determined from typical EFIT equilibria. A vertically-distributed four-hole gas puffer was located just outside the midplane viewing region of Fig. 1. The images were transmitted to a Phantom 710 camera using a 57×57 pixel coherent quartz fiber optic bundle inside a long bellows. The spatial resolution of the whole optical system was ~ 2 - 3 mm for objects in the midplane view.

Initial results from the X-region view were described briefly [12], so more details of the hardware are described here. A second in-vessel telescope was mounted on the outer wall and pointed at the center of the X-region view of Fig. 1 in the local B field direction, which was 4° below horizontal, as determined from typical EFIT equilibria. This telescope was 43° toroidally from the center of the X-region gas puff at a distance of 0.73 meters. A design study showed that variations in the local B field angle over the X-region view were $\pm 1^\circ$ over a ± 3 cm variation in R, and $\pm 1.5^\circ$ over a ± 3 cm variation in z; thus the local B field direction varied by only about $\pm 2^\circ$ over this field of view. The gas puff nozzle for this view was a single-hole capillary tube located in a divertor-target tile at the wall ~ 3 cm below the bottom of the X-region view [12]. The helium gas to this view was triggered independently from the midplane GPI gas puff. The telescope optics, fiber optic bundle, and camera for the X-region view were similar to the midplane view, and the spatial resolution of the whole optical system was also ~ 2 - 3 mm.

The main difficulty with the X-region view was the relatively large background light from the lower divertor region behind the X-region view. The best solution to this problem was to use helium gas in the GPI (with deuterium plasmas), as was done in the present experiment, although some deuterium GPI results were obtained with double-null deuterium discharges, as reported previously [12]. Another problem was breakage of the insulating section of the capillary tube which was needed to electrically isolate the X-region GPI gas nozzle; this was solved by using a commercial alumina-to-stainless isolator (CeramTec). The X-region nozzle was put as close as possible to the X-region GPI view, but this distance (~ 3 cm) was farther than the distance from the midplane nozzle to the edge of the midplane view (~ 0.1 cm).

C. GPI diagnostic operation

All data in this paper were taken using helium GPI puffs viewed with He I (587.6 nm) line filters. A total of 6-8 Torr-liters (~ 2 - 3×10^{20} atoms) was puffed over ~ 200 - 300

msec, about half going to each GPI view. The two Phantom 710 cameras were always operated at 391,000 frames/sec with a frame separation time of $\sim 2.6 \mu\text{s}$, an exposure time of $\sim 2.1 \mu\text{s}$ /frame, with a 64x64 pixel format for this experiment. Since the majority gas was deuterium in all cases, the GPI HeI signal was nearly zero in both views before the puff. These GPI signals rose with the puff over ~ 30 msec, and stayed fairly constant for the next ~ 50 -100 msec. Camera data was acquired for 60,000 frames/shot over ~ 150 msec (~ 0.4 GB per camera per shot).

Figure 2 shows typical single frames of the (normalized) GPI light signals for the X-region view (left) and midplane view (right), taken at the same time in the same shot with a camera exposure of $\sim 2.1 \mu\text{s}$. Also shown are the separatrix locations (solid line) and SOL flux surfaces at $\rho=1$ cm and 2 cm (dashed lines), taken from EFIT equilibria. The false-color scale of Fig. 2 ranges from 0.5 (black) to 1.5 (white), where each pixel has been normalized by its time average over ~ 4 msec, and the pixels with low average signal levels (≤ 25 counts) are shown as black. Un-normalized signal levels near $\rho=1$ cm are typically ~ 100 -200 counts in the midplane and ~ 50 -100 counts in the X-region, and useful GPI data in these experiments typically covered the radial region from ~ 0.5 cm inside the separatrix to ~ 2 cm outside the separatrix. The radial range of useful GPI data varied with the location of the separatrix with respect to the gas nozzles, but a typical case is illustrated in Fig. 2. The inner edge of the shadow of the innermost outboard limiter (located at a different toroidal angle than the GPI) is shown by the black line in the midplane view, and cross-sections of the divertor plates at the focal plane of the X-region view are outside its view (the divertor target plates behind the gas puff in this downward-pointed X-region view are viewed out-of-focus).

Note that since the optical sightlines are aligned (nearly) along the local direction of the total B at these two locations, the images in Fig. 2 show the turbulence in the plane perpendicular to B , i.e. in the radial vs. poloidal (i.e. binormal) direction. Therefore in this paper the word ‘poloidal’ refers to the direction perpendicular to the total B and also perpendicular to the radial direction across magnetic flux surfaces.

D. Database and overview of data

The database of shots used in this experiment is shown in Table 1. All shots are deuterium fueled, lower-single-null diverted discharges. The times of interest for the GPI analysis were chosen during steady-state periods to avoid transient events such as L-H transitions, ELMs, and variations in RF heating. The range of plasma parameters was toroidal field $B_0=4.2$ -6.0 T, plasma current $I=0.73$ -1.0 MA, $q_{95}=3.3$ -5.0, and line-averaged density $n=1.0$ - $3.6 \times 10^{20} \text{ m}^{-3}$, all of which are within the normal range of C-Mod operation. These densities spanned a range of values normalized to the Greenwald density of $\sim 0.2n_G$ (1120224), ~ 0.5 - $0.8n_G$ (1120712), and $\sim 0.5n_G$ (1120815).

These shots occurred during three different run days in 2012. Typical SOL plasma parameters for the first and third run days are summarized in Table 2, which are in the normal range for C-Mod [51]. The first run (1120224) consisted of RF-heated

discharges at low-to-moderate density. Some data were taken in L-mode but close to the L-H transition, and others in a brief ELM-free H-mode [48]. Cases examined in the second run (1120712) consist of Ohmic EDA H-modes initiated by toroidal field ramps. Some of the Ohmic H-modes had short-wavelength magnetic perturbations injected at the edge by a ‘shoelace’ antenna [49], although these perturbations are not thought to have substantially affected the edge turbulence. The third run (1120815) examined RF-heated ELMy H-modes [50]. There were at least two different RF antennas active for the first and third run days. The equilibria were slightly different for each run, e.g. the distance between the separatrix and the outer midplane limiter was ~ 1.1 - 1.7 cm for the RF runs 1120224 and 1120815, but only ~ 0.1 cm for Ohmic run 1120712. In the Ohmic run, the SOL was relatively narrow and the field lines outside $\rho \sim 0.5$ - 1.0 cm were intercepted by limiters before they reached the divertor plates. However, in all cases both GPI systems had good signal levels out to at least $\rho \sim 2$ cm into the SOL.

Sample movies of the normalized turbulence images in the same format as Fig. 1 are located in the ‘‘Supplementary Information’’ files for this paper, and also on a public web site at [52]. These movies show a complex turbulent structure and motion in both the midplane and X-region views. The turbulence structures have a typical size scale of ~ 1 cm in both views, but the shapes appear more elongated in the major radial direction in the X-region view compared with the midplane view. The turbulence motion does *not* look like a ‘frozen flow’ on space-time scale of these images, but the turbulence usually moves at least one correlation length before changing shape, similar to clouds moving across the sky. There is sometimes a relatively uniform poloidal drift velocity of the turbulence over each these views (e.g. in the X-region of 1120224009), but normally the poloidal velocity varies somewhat as a function of radius and time. There is generally no clear correlation visible by eye between the poloidal turbulence motion in the two views (as discussed quantitatively in Sec. IV). The radial component of the turbulence velocity is generally smaller than the poloidal component, except for the Ohmic plasmas in which it can be dominant, and a radially outward motion is much more common than an inward radial motion. There is no immediate (i.e. sub-millisecond) change in the turbulence structure or velocity with the turn-on or turn-off of RF heating, but there are complex variations during ELMs and L-H transitions, which are not treated in the present paper.

E. Turbulence structure analysis

The structure of the turbulence was analyzed by first normalizing (i.e. dividing) each 64×64 pixel frame by the time-averaged frame for that shot over 3-5 ms (1200-2000 frames), and then smoothing the results for each frame over 3 pixels in space (~ 0.3 cm) to reduce the random noise level. Only regions with relatively large signal level were used, which limited the analysis to between ~ 0.5 cm inside the separatrix to ~ 2 cm outside the separatrix. After normalization, the cross-correlation coefficient between any chosen pixel and all other pixels in the image was calculated by averaging over the time of interest. Starting from the chosen point where the cross-correlation was 1.0, one dimensional cross-correlation functions were then calculated for each rotation angle in the image plane (in 1° increments), and for each rotation angle the length over which the

correlation coefficient was ≥ 0.7 was evaluated, in order to find the shape of the highly correlated part of the turbulence structure. The maximum and minimum of these lengths for any rotation angle were used to characterize the turbulence size at that pixel location. The angle of the maximum length was used to characterize the turbulence tilt angle, and the ratio of the maximum length to the length at 90° to this maximum was used to characterize the turbulence ellipticity. This analysis of X-region images was also used in [12]. The results of this analysis are in Sec. IV.B.

A separate analysis of the tilt angle and ellipticity was done using discrete blob structures, similar to that done previously for NSTX GPI data [27]. The images were first normalized and smoothed as above. Then resulting images were contoured at 1% intervals, and the closed contours which fit certain assumed size constraints were considered to be blobs. The contour midway between the lowest and highest level contours was fit with an ellipse. The ellipticity, size, tilt angle, height and location of the peak of these blobs are recorded for each frame. The blobs were tracked from frame-to-frame given certain constraints such as a maximum displacement of 10 pixels per frame, corresponding to a maximum speed ≤ 3.2 km/sec, and blob speeds and lifetimes were then recorded. The results from the blob analysis are similar to the cross-correlation analysis.

F. Turbulence velocity analysis

The time-averaged turbulence velocity was evaluated at any given pixel by first normalizing and smoothing the images as above, and then evaluating the time-delayed cross-correlation coefficient from that pixel using ± 8 adjacent pixels in either direction (i.e. ± 0.7 cm) for time delays of up to ± 10 frames (i.e. ± 25 μ s). For each time delay the 2-D velocity was evaluated as the 2-D distance to the pixel of maximum cross-correlation divided by that time delay, and the velocity for that pixel was the average over all the time delays which had a cross-correlation coefficient above 0.5 (but only if there were at least four time such time delays). This process only finds local velocities within the range ± 2.8 km/s in either direction, but essentially all velocities found this way were well within this range (i.e. ≤ 1.5 km/sec). These velocities were sometimes averaged over 0.5 cm wide radial zones using every third pixel in either direction, as described in Sec. IV.C. These averages were very similar when using every pixel or every third pixel.

The time-dependent turbulence velocity for each pixel was calculated separately in order to look for common fluctuations in the poloidal flow between the midplane and X-region (i.e. zonal flows), as done previously for the midplane data [16]. For this calculation the time series for each pixel were first divided into bins of ± 5 frames (25 μ s), and the 2-D velocities were then calculated using a threshold correlation coefficient of 0.8 for a single time delay of one frame (2.5 μ s), since this computation is very long. These time-dependent velocities were then averaged over 0.5 cm wide radial zones, and results were cross-correlated between the midplane and X-region, as described in Sec. IV.D. The longer-time (50 ms) evolution of the velocity at typical points was also evaluated using 10 time segments of 5 ms each, as described in Sec. IV.E.

G. Limitations and uncertainties

This GPI diagnostic and data analysis have many limitations and uncertainties. First of all, this diagnostic measures only HeI neutral light, which can respond to both electron density and temperature fluctuations [45-47]. Thus the relative fluctuation level in the GPI signal is not simply proportional to the density fluctuation level. If the electron density and temperature fluctuations are different from each other, the GPI will measure some complicated mixture of the two; thus we assume that electron temperature and density fluctuations are well correlated. We also assume that the He neutral density is not fluctuating on the space-time scale of the turbulence, although there could be some shadowing effect due to the turbulence itself [45]. On the other hand, there is good evidence that the GPI turbulence signals in the SOL correlate well with Langmuir probe turbulence signals when measured on the same field line, for example in C-Mod [19] and NSTX [53], and TPE-RX [54].

The analysis of the turbulence structure as described in Sec. III.E assumes that the GPI telescope is viewing exactly along the local B field at the gas cloud. The actual field line angles (according to EFIT) in this experiment were 8.5-12° below the toroidal direction for the midplane view, and 3.5-5° below the toroidal direction for the X-region view, which are within ~2° degrees of the telescope sightlines of 11° and 4°, respectively. The degradation of the spatial resolution of the GPI images depends on the misalignment angle and the length of the sightline through the GPI gas cloud. A simulation of the toroidal extent of the GPI gas cloud using DEGAS 2 gave a cloud FWHM of ~6 cm for the midplane view [33], and a separate simulation of the X-region GPI view gives a toroidal extent of ~4 cm at the bottom (low-z) edge of the view, 8 cm at the center, and ~11 cm at the top (these results are nearly the same for deuterium and helium). Therefore these misalignments should result in a point-source spread of ≤ 0.3 cm in these images, which is comparable to the spatial resolution of the diagnostic, and so should have a relatively small effect on the size and orientation of the ~1 cm turbulence structures in this experiment. As described in [12], if the gas cloud somehow had a toroidal extent of 20 cm FWHM, it would result in measured elongations that are longer and tilts that are significantly more horizontal than the actual cross-sections of structures in a single toroidal plane.

The analysis of the turbulence velocity described in of Sec. III.F has several important limitations, most of which have been discussed previously [55]. This method cannot detect flows along the direction of constant GPI intensity, or resolve separately counter-propagating flows, and can not measure the phase velocity of these perturbations. This particular cross-correlation method detects only velocities ≤ 2.8 km/sec, which can miss some faster moving flows in the far-SOL that exist during RF heating [17], or faster flows near or inside the separatrix. However, this method does correctly track the 2-D velocity of small-scale features, similar to the way the wind speed can be inferred from moving clouds. This turbulence velocity is *not* necessarily the same as the ExB fluid (ion) flow velocity, since there also may be turbulence propagation in the rest frame of the plasma, as discussed in Sec. V.C.

Some other limitations of the cross-correlation method for velocity analysis have been described recently [20,56,57]. There are fundamental ambiguities in velocity estimates made using 1-D cross-correlations in a 2-D velocity field; however, the method of Sec. III.F uses a 2-D cross-correlation analysis, so should be relatively immune to these difficulties, subject to the limitations discussed in [55]. There can also be significant sources of noise in the time-dependent evaluation of turbulent velocity, e.g. for estimating zonal flows; however, velocity fluctuations are not the main focus of the present paper.

The separatrix and SOL flux surface locations were calculated using EFIT equilibrium reconstructions and not directly measured in these experiments. Recent analysis of C-Mod probe data [18] indicated that flux surface shifts of ~ 0.1 - 0.5 cm were required to match the horizontal probe data just above the outer midplane, and ~ 0.1 cm shifts were required to match the vertical probe near the X-region GPI poloidal location. For displaying radial profiles, the GPI data was binned in 0.5 cm radial zones in this experiment.

A general uncertainty in this paper is whether the GPI gas puff can significantly perturb the local plasma or turbulence as measured by the GPI. It is difficult to resolve this uncertainty directly, since there were no other SOL measurements in C-Mod at the same place and time as the GPI. Although there was a high correlation between the turbulence seen by GPI and a Langmuir probe located on nearly the same B field line [4,19], this does not exclude the possibility that one or both of these diagnostics were perturbing the turbulence. Since there were two helium puffs in these experiments, there was a sometimes relatively large increase in the line-averaged density sometimes of up to 10-20% due to these puffs. However, such density changes are comparable to the shot-to-shot variation in this experiment and do not imply any unusual perturbation of the edge turbulence. There were no systematic changes in the turbulence seen in the GPI as a function of time during the puff, indicating that the observed turbulence did not depend on the rate of gas influx. There were no systematic changes in global parameters such as the stored energy, radiated power, loop voltage or MHD activity due to these puffs.

A rough estimate of the perturbing effect of the GPI puff can be made based on the energy and particle flow into the magnetic flux tubes containing this puff, since the plasma parameters and turbulence are presumably determined by B-field line averages. The source rate of helium from the midplane GPI gas puff is $\sim 10^{21}$ neutrals/sec over a poloidal length ~ 6 cm at the outer midplane separatrix, while the plasma heat and particle flux most likely occurs over a poloidal length of roughly ~ 60 cm at the outboard separatrix. The expected radiation loss for a helium atom is ~ 100 eV, and the power needed to heat the neutrals to the SOL temperature is ~ 30 eV. Thus the energy loss due to the puff is ~ 10 - 20 kW, while the plasma energy loss across the poloidal range of the puff is roughly $\sim 10\%$ of the total heating power, i.e. ≥ 100 kW; therefore the radiative cooling effect of the puff on the field line should be small. The plasma ion loss across the poloidal range of the puff is harder to estimate but is probably $\sim 10^{21}$ ions/sec, which is comparable to the helium puff rate. Thus these puffs might well perturb the density on the local SOL field line, although measurements of this were not available on C-Mod.

The neutral density in the GPI viewing region is certainly increased by the puff, but large neutral density perturbations in the edge of C-Mod are common due to limiters and RF heating, particularly near the divertor region. Since the sensitivity of the SOL turbulence to plasma or neutral perturbations is basically unknown, there is still some uncertainty about the effects of the GPI puff on the turbulence measured in this experiment.

IV. Experimental Results

This section uses the analysis methods of Sec. III applied to the database of Table 1. Section IV.A compares the basic characteristics of the turbulence in the midplane and X-region views. Section IV.B compares the 2-D (radial vs. poloidal) spatial structure of the turbulence in these two views, and section IV.C compares the time-averaged 2-D velocity of the turbulence. Section IV.D describes the time-resolved velocity analysis, and Sec. IV.E discusses longer time evolution in the data.

Note again that these two GPI views were *not* designed so as to view the same magnetic field line in the SOL, and there was almost never any significant cross-correlation between the turbulence seen in these two views (see Appendix). Thus the comparisons between the midplane and X-region turbulence described below are based on statistical differences in the average turbulence structure and velocity between them.

A. Basic turbulence characteristics

Figure 3 shows some comparisons between the turbulence seen in the X-region and midplane GPI views for three typical shots, one from each of the run days of Table 1. The horizontal coordinate is the radial distance ρ outside the separatrix, as measured at the outer midplane (positive into the SOL). At the top are radial profiles of the relative GPI fluctuation levels (standard deviation/mean), averaged over radial flux surface zones of 0.5 cm width, and in the middle are the autocorrelation times (FWHM), averaged over the same regions. At the bottom are the frequency spectra (FFT amplitude) averaged over smaller regions near the center of the images at $\rho=1$ cm. The data for each shot were time averaged over 3-5 msec during the steady-state part of these discharges in the absence of transient events. The low frequency peak in the midplane signal for 1120224022 at ~ 4 kHz is due to an edge mode, as discussed in Sec. IV.D.

The relative fluctuation levels are all fairly large (~ 10 -40%), the autocorrelation times are all relatively short (~ 10 -50 μ s), and the frequency spectra are all relatively broad (~ 1 -100 kHz), all similar to those seen previously in the midplane GPI in C-Mod [8,16] and in the SOL of other tokamaks [1,2]. There is a possible trend for a larger autocorrelation time in the X-region compared with the midplane region. The probability distribution functions of the signal amplitude are near Gaussian in these cases, but have stronger positive skewness outside $\rho=2$ cm, as seen previously on C-Mod and elsewhere. Thus the basic turbulence characteristics were roughly similar in the outer midplane and X-region as seen in the GPI data.

B. 2-D Spatial structure

Figure 4 shows typical 2-D spatial cross-correlation functions calculated for the midplane and X-region views with zero-time delay, and plotted in the same format as for the raw data in Fig. 2. These cross-correlation functions are calculated from the two points shown by the black “x” marks, which were both at a radius $\rho = 1$ cm in the SOL. The color scale in Fig. 4 follows the color bar at the right. The raw data was smoothed over ~ 0.3 cm before cross-correlation and time-averaged over 3 msec (1200 frames).

The cross-correlation function for the outer midplane in Fig. 4 has a size of ~ 0.5 - 1.5 cm FWHM, similar to that described previously for GPI in C-Mod [8,16]. The X-region cross-correlation appears elongated horizontally, i.e. in the major radius direction, similar to the initial deuterium GPI results for double-null discharges in this view [12]. There were often regions of negative cross-correlation about 1 cm radially inside or outside the peak correlation in both views, such as shown in blue in Fig. 4, but these are not universal in this dataset.

Figure 5 shows examples of 2-D shapes of such cross-correlation functions over the X-region (left) and midplane (right) views for four typical shots. These maps are drawn for the same regions as Figs. 2 and 4 and oriented in the same direction. For both maps the separatrix is shown by the solid line and flux surfaces in the SOL are shown by the dashed lines at 0.5 cm radial intervals out to $\rho=2$ cm. The elliptical structures are defined by the shape and tilt direction of the 2-D correlation functions at a correlation of 0.7, averaged over the time intervals in Table 1 (see Sec. III.E). The size of these ellipses is reduced by a factor of three with respect to the images so that the ellipses do not overlap. The size and tilt direction of these correlation ellipses is roughly consistent within a given viewing region for a given shot, but there are sometimes significant variations in shape and direction, particularly near or inside the separatrix and outside $\rho=2$ cm. The gray central regions at $\rho=1$ cm are used for a larger database below.

Figure 6 shows a comparison between the turbulence correlation lengths and areas in the midplane and X-region, with one point per shot sorted in color according to run day. These lengths are based on data like that in Fig. 5 averaged over central regions of each view near $\rho=1$ cm, as shown by the gray areas in Fig. 5 (± 0.6 cm for runs 1120224 and 1120815 and ± 0.3 cm for 1120712). At the left are the maximum lengths of the correlation function in any direction within the 2-D image plane, which were similar between the midplane and X-regions (~ 1 - 2 cm). In the middle are the minimum correlation lengths in any direction, which were somewhat smaller in the X-region. The product of these lengths, i.e. the area of these correlation structures, was somewhat larger in the midplane region, as shown at the right. The turbulence area in the X-region is roughly 0.8 times that in the midplane view, as indicated by the ‘slope 0.8’ line.

Figure 7 shows a parameterization of the shapes of the 2-D turbulence structures for pixels within the same central regions as used for Fig. 6 and shown in gray in Fig. 5. However, for this plot the structure analysis is done for 9 separate points within each of these central regions, and the results are shown separately for each run day. The tilt

angles plotted on the vertical axis is the angle at which the cross-correlation function had its maximum length, as measured counter-clockwise from the horizontal major radius direction. The ellipticity plotted on the horizontal axis is the ratio of this largest length to the length perpendicular to this direction (which is nearly the same as the minimum length). The solid symbols in Fig. 7 were based on cross-correlation analysis as used for Fig. 6, while the open symbols were based on a separate blob structure analysis for each shot (see Sec. III.E). The tilt angle of the local magnetic flux surfaces with respect to the horizontal (major radius) direction are shown by the horizontal bars in each case.

Despite the considerable (real) scatter, Fig. 7 shows a consistent difference between the tilt of these structures in the midplane and X-regions. The major axis of the cross-correlation ellipse is fairly well aligned with the local flux surfaces in the midplane view, with an average tilt of the major axis of the cross-correlation ellipses of $16 \pm 7^\circ$ (clockwise) from the local flux surfaces, averaged over all shots. However, the average tilt of the cross-correlation functions is $42 \pm 7^\circ$ (clockwise) from the local flux surface for the X-region view, as was illustrated in Fig. 4. Thus the turbulence structures are rotated $\sim 25^\circ$ more (clockwise) with respect to the local flux surfaces in the X-region view than in the midplane view, at least near the $\rho=1$ analyzed here. Note that a perfectly circular flux tube at the outer midplane develops a slight clockwise tilt even at a small distance below the midplane (see Fig. 1), similar to the tilt in the midplane GPI view in Fig. 7.

The average ellipticity for the central image region of Fig. 7 is 1.7 ± 0.3 for the midplane view and 2.1 ± 0.3 for the X-region view, which is marginally larger for the X-region. This increase in ellipticity in the X-region is qualitatively similar to the flux tube maps shown in Fig. 1, assuming that the turbulence is nearly isotropic near the outer midplane.

In summary, the tilt of the turbulent structures in the (R,z) plane was significantly different between the midplane and X-region, and the area and elongation of the structures were slightly different in these two regions. A discussion of these results with respect to the magnetic flux tube model is in Sec. V.B.

C. Time-averaged turbulence velocity

The time-averaged 2-D turbulence velocity fields in both the midplane and X-region images were evaluated using the time-delayed cross-correlation method described in Sec. III.C. This analysis was done for every shot in Table 1 for the time periods of 3-5 msec per shot (1200-2000 frames). This section describes these time-averaged velocities, while the time-dependent velocities are described in Sec. IV.D, and the longer-time evolution is described in Sec. IV.E.

Figure 8 shows 2-D maps of the velocity vectors for the X-region (left) and the midplane (right) for four typical shots. The orientation is the same as for Fig. 5, overlaid with the separatrix (solid line) and SOL flux surfaces at 0.5 cm radial intervals (dashed lines). Velocity vectors are shown for every third pixel for the regions with good signal

levels, as in Fig. 2. These vectors are drawn with a maximum velocity for each shot specified in the corner of each image, and scaled according to this velocity for each image separately. The velocities at the edges are not shown because the full correlation search over ± 8 pixels could not be completed. The central gray areas are also used for some of the analysis below.

These time-averaged velocity maps show complex flow patterns which can vary significantly between these two GPI views. In some cases like 1120224009 (top), the direction of the turbulence velocity is largely constant within the SOL of each view, but the direction with respect to the local flux surfaces is different between the two views, i.e. with relatively larger radial component in the X-region. The midplane velocity vectors can be either upward as in 1120224009 (electron diamagnetic direction), or downward as in 1120224022. The X-region velocities can vary significantly in both direction and magnitude; for example, there appears to be a circulation in the X-region near $\rho=1$ cm in 1120224022 and outside $\rho=2$ cm in 1120815021, but these two circulations are in opposite directions. There is occasionally a localized change in direction within a distance of a few centimeters, such as in the X-region near $\rho=1$ cm for 1120712026, and in the midplane outside $\rho=2$ cm in 1120815021. However, there are also similarities in the velocity fields within a given run day; for example, shots 1120224015, 112022423 and 1120224024 look qualitatively similar to 1120224022, 1120224027 looks similar to 1120224009, and all four shots within runs 1120712 and 1120815 look qualitatively similar to each other. It is likely that some of the consistent run-to-run variation is due to the presence or absence of ICRF heating and the magnetic mapping from each view to the active antennas, since it has been shown [17] that large potentials are induced by the ICRF on flux tubes that pass close to or intersect active antennas. The ICRF-induced radial electric fields were shown to affect strongly the phase velocities of fluctuations (via $E \times B$) in regions that map magnetically to near the antenna structures. The qualitative effects of the ICRF on SOL flows will be discussed further in Sec. V.C.

Figure 9 shows comparisons of the radial profiles of poloidal velocities V_{pol} between the midplane and X-regions, found by averaging over radial zones of width 0.5 cm in maps like those of Fig. 8. Each point in Fig. 9 represents one shot and has an error bar showing the standard deviations of V_{pol} over the ~ 20 -30 pixels in that radial zone for that shot (note the different vertical scales). The lines shown are cubic spline fits of the midplane and X-region data separately. The V_{pol} profiles of the shots for 1120224 are significantly different between midplane and X-region views (i.e. largely outside the mutual error bars), with a dominantly positive (electron direction) turbulence velocity in the X-region view and a dominantly negative turbulence velocity in the midplane view. The average poloidal velocities in the midplane and X-region velocities in runs 1120712 and 1120815 are considerably smaller than for 1120224, but the variations within each radial zone for each shot (i.e. the error bars) are comparable to the time-averaged velocities. The small-scale details of the velocities are not the same in the two fields of view, as illustrated in Fig. 8.

Figure 10 shows the same data as in Fig. 9 but now with the midplane velocity plotted vs. the X-region velocity for each radius for each shot. At the left are the poloidal

velocities and at the right are the radial velocities, sorted in color by run day as for Fig. 6. There is a partial linear correlation (59%) between V_{pol} in the midplane and V_{pol} in the X-region, although the velocity is often negative in the midplane while positive in the X-region. The radial velocities are almost all positive (radially outward), but significantly smaller than the poloidal velocities (note the change in velocity scales). There does not seem to be any linear correlation between radial velocities in the midplane and X-region, and the few negative radial velocities are only for points near the separatrix. Note that even though the time-averaged velocities in Figs. 9 and 10 are sometimes nearly zero, the small-scale turbulence structures are still in motion but without any consistent direction, as can be seen in the movies [52].

In summary, there were significant differences in the turbulence velocity between the midplane and X-regions even within same flux surfaces in the same shot. There were also complex velocity variations within both regions for a given shot, and significant differences from run-to-run. It is not clear at this point what causes these difference in velocity within each field of view, or from run-to-run. Possible interpretations of these velocity results are discussed in Sec. V.C.

D. Time-dependent turbulence velocity

It is interesting to examine the fluctuations in poloidal velocity δV_{pol} to see if they are correlated between the X-region and midplane views, as would be the case for zonal (i.e. $n=0$, $m=0$) flows. In the previous analysis of midplane GPI camera data for C-Mod [16], most shots showed only a broadband turbulent δV_{pol} frequency spectrum over ~ 1 kHz - 40 kHz, although the shots at the lowest line-averaged density ($n \leq 1 \times 10^{20} \text{ m}^{-3}$) showed had a coherent δV_{pol} oscillation at ~ 6 kHz within ± 1 -2 cm of the separatrix. The same analysis procedure was applied to the present data (see Sec. III.F).

Figure 11 shows a case in which there was a clear oscillation in V_{pol} in both the midplane and X-region GPI views, which was also correlated with a $D\alpha$ light fluctuation (left). These velocities were obtained by averaging over all pixels in the radial zone from 0-0.5 cm, as done in Figs. 9 and 10. In this case (1120224024) the oscillation is at 2.3 kHz, as shown in the GPI $D\alpha$ signal spectra at the right. Similar but weaker edge oscillations in the frequency range ~ 2 -5 kHz occurred for many of the shots in the run of 1220224 (but not in 1120224022). These coherent velocity oscillations are much less apparent in individual pixels, which are dominated by turbulence velocity fluctuations or random correlation noise. A more detailed discussion of this edge oscillation will appear elsewhere [48].

Figure 12 shows an analysis of the cross-correlation of the δV_{pol} fluctuations between the midplane and X-region views as a function of radius for all shots in Table 1, where δV_{pol} in each view was averaged over 0.5 cm in radius for each shot. The vertical axis is the maximum value of the cross-correlation function found by searching over a time lag of up to ± 800 μsec and averaging over the analysis time of ~ 3 -5 msec. The two shots with maximum cross-correlation above 0.3 were both H-mode cases with a low

frequency edge mode (e.g. 1120224024). For almost all the other shots the maximum cross-correlation was ~ 0.10 - 0.15 , which is not significant since the maximum cross-correlation of these zones between two different shots is ~ 0.09 - 0.13 (due to random coincidences). These include L-modes cases which also had a low frequency edge mode (e.g. 1120224027).

In summary, most shots in this database did not have any correlated fluctuations in the poloidal velocity of the turbulence between the midplane and X-region views. However, a few of the shots on one run day (1120224) did have a low frequency coherent oscillation in the SOL which was correlated between the midplane and X-regions. This oscillation will be discussed in more detail elsewhere [48].

E. Longer-time evolution

The relatively short 3-5 ms time intervals shown in Table 1 for the analyses of Secs. IV.A-D were chosen to give a sampling of the behavior during the steady-state plasma current and heating periods when there was no large MHD, L-H transitions, ELMs or other obvious transient events. A much longer 50 msec time evolution for three typical shots is shown in Fig. 13, for which the same analyses were done for 10 successive time periods of 5 msec each. These analyses were done using only one central pixel at $\rho=1$ cm, such as shown by the “x’s” in Fig. 4. The time axes are relative, and the times used for the shorter analyses of Table 1 are shown by the boxes just above the horizontal axis.

For two of the three shots in Fig. 13 (1120224027, 1120712029) the correlation tilt angle and poloidal velocity were nearly constant over 50 msec, as were the ellipticity, turbulence correlation size, and radial velocity (not shown). The first of these shots (1120224027) was in L-mode with 3 MW of RF heating and had small ~ 4 kHz frequency coherent edge oscillations (see Sec. IV.D), and the second of these was an Ohmic EDA H-mode plasma with no such oscillations. The 2-D maps of turbulence structure and velocity for these two shots were also nearly (but not perfectly) the same over 50 msec. The third shot of Fig. 13 (1120815021) was in H-mode with 2 MW of RF heating, and had a series of small ELMs which perturbed the GPI signal occasionally for ~ 1 msec periods during the 50 msec interval of Fig. 13. During the time segments with ELMs the tilt angle (averaged over 5 msec) was sometimes transiently increased, e.g. at 5 msec and 20 msec in the X-region, and at the three later times in the midplane region. Note that the analysis times in Table 1 for the shots of 1120815 did not contain ELMs.

In summary, the longer-time behavior of turbulence in both the midplane and X-regions was similar to the shorter analyses of Sec. IV.A-D, except during ELMs. There were also interesting variations in the turbulence at L-H transitions, which will be discussed separately [58]. Further analysis of the time dependence during such transient events is beyond the scope of the present paper.

V. Discussion and Conclusions

This section discusses the results of Sec. IV with respect to theory and to previous experiments. Section V.A is a discussion of the basic turbulence characteristics, Sec. V.B is a discussion of the turbulence structure, and Sec. V.C is a discussion of the turbulence velocity (corresponding to the experimental results in Sec. IV.A, B, and C). The relationship between the turbulence structure and velocity is discussed in Sec. V.D, and several additional physics issues are discussed in Sec. V.E. The relationship of these results to previous experiments is discussed in Sec. V.F, and Section V.G presents the conclusions and suggestions for further research.

A. Discussion of basic turbulence characteristics

The main result of Sec. IV.A and Fig. 3 was that the turbulence fluctuation levels, autocorrelations times, and frequency spectra in the midplane and X-region views were similar to each other. In both views the relative fluctuation levels were large ($\sim 10\text{-}40\%$), autocorrelation times were small ($\sim 10\text{-}50\ \mu\text{s}$), and the frequency spectra were broad (1-100 kHz). There was sometimes a low frequency coherent oscillation in the GPI signals at $\sim 2\text{-}5\ \text{kHz}$ which was common to both views (Figs. 11-12), which will be discussed separately [48].

These turbulence characteristics should be interpreted with 3-D simulations, but no new simulations of the C-Mod SOL are presently available. Previous SOL turbulence simulations for C-Mod done using the BOUT fluid code showed some similarity to the measured SOL turbulence at both the outer midplane [32] and in the X-region [12]. Gyrofluid SOL simulations for C-Mod were compared with the outer midplane SOL turbulence, but only for a circular limited C-Mod plasma [33], and 2-D SOLT simulations were compared with EDA H-mode plasmas in C-Mod [27,59]. On other devices, 3-D turbulence simulations have been compared with experiments on TORPEX [34] and DIII-D [35], but it is not clear whether those results apply to the SOL conditions in C-Mod.

In the absence of relevant turbulence simulations, some rough connections to theory can be made for typical SOL parameters for this experiment. The parameters of Table 2 were obtained from the edge Thomson scattering data averaged over $\rho=0\text{-}1\ \text{cm}$ for two of the run days of Table 1. The relative density fluctuation levels can be compared with the ‘mixing length limit’ of $\tilde{n}/n \sim 1/(k_{\text{rad}}L_n)$, where k_{rad} is the typical radial turbulence scale length and L_n is the radial density scale length. In this experiment, $k_{\text{rad}} \sim (\text{correlation length})^{-1} \sim 1\text{-}2\ \text{cm}^{-1}$ (Fig. 6) and so for $L_n \sim 1\text{-}2\ \text{cm}$ (Table 2), this implies a fluctuation level on the order of ~ 0.5 , which is qualitatively consistent with the GPI fluctuation levels of Fig. 3. The size scale ($k_{\text{pol}}L_n \sim 1$ and $k_{\text{pol}}\rho_s \sim 10^{-2}$) and frequency range of this turbulence is at least qualitatively similar to that seen in previous SOL turbulence simulations [32-35]. The SOL in these plasmas is highly collisional ($v_{e*} =$

$L_{II}/\lambda_e \sim 100$) and the beta is very low ($\sim 3 \times 10^{-5}$), so the turbulence is most likely dominated by resistive electrostatic instabilities.

B. Discussion of turbulence spatial structure

The main result of Sec. IV.B and Figs. 4-7 was that the tilt of the turbulent structures in the (R,z) plane was significantly different in the midplane and X-region, and the area and elongation of the structures were slightly different in these two regions. This section compares these results with a simple magnetic flux tube model. This model assumes that the turbulence structure follows magnetic flux tubes toroidally and poloidal around the SOL, such as illustrated in Fig. 1.

Figure 14 compares the measured turbulence structure with the magnetic flux tube model for a specific shot (1120224022). The experimental data points are the same as shown in Fig. 7 for the central region near $\rho=1$ cm (i.e. the gray areas in Fig. 5), but now labeled with triangles for the cross-correlation analysis and open circles for the blob analysis, with error bars showing the standard deviations in this region. The solid colored ellipses show the tilt (measured with respect to the major radius direction) and the ellipticity of magnetic flux tubes in this plane. These flux tubes are started with a range of tilt and ellipticity overlapping the measured values in the midplane (top), and are ended when they reach the (R,z) coordinates of the X-region view (bottom). If the turbulence followed magnetic field lines, the measured X-region tilt and ellipticity should agree with the calculated flux tube shapes for the X-region based on the field line mapping from the midplane.

The result of Fig. 14 is that there is partial (but far from perfect) agreement between the observed X-region turbulence structure and the simple magnetic flux tube model. The measured tilts in the X-region are nearly in the major radius direction ($\sim 0^\circ$), whereas the calculated tilts are $\sim 20^\circ \pm 10^\circ$ downward, such as shown in Fig. 1. The measured ellipticity in the X-region is ~ 2 , whereas the calculated ellipticity is $\sim 4 \pm 2$. There is a similar level of (dis)agreement of the observed X-region structure with the flux tube model for two other shots from other run days in this experiment. These differences can not be accounted for by variations in the radial location of the assumed flux surfaces in the model over $\rho=1.0 \pm 0.5$ cm, which are typically $\pm 5^\circ$ in tilt and ± 0.4 in ellipticity. Some distortions in the observed turbulence structure may also be caused by the slight misalignments of the viewing angle with respect to the local B field, as discussed in Sec. III.G, but these do not seem to be large enough to cause the disagreement between the data and the model for the X-region in Fig. 14.

Another point of comparison between the turbulence structure and the flux tube model is the relative spatial scale of the turbulence in the two regions. The measured area of the structures was shown in Fig. 6 was roughly 0.8 times smaller in the X-region than in the midplane view, which is similar to the expected area ratio of ~ 0.8 if the turbulence followed magnetic flux tubes ($R_X/R_{\text{mid}} \sim 0.78$), although there is a considerable scatter in the data. The maximum length of the flux tube cross-sections in Fig. 14

increases by a factor of ~ 2 from the midplane to the X-region, but the measured turbulence structures do not significantly increase in maximum length, which disagrees with this model. Thus the overall result is only a partial agreement with the simple magnetic flux tube model.

There are several possible reasons why the magnetic flux tube model may not explain the observed variations of the turbulence structure between these two viewing regions. First, possible changes in turbulence structure due to $E \times B$ shear are not taken into account, as discussed in Sec. V.D. Second, the model assumes that the turbulence in these two toroidally-separated viewing regions has the same structure, which may not be correct due to non-axisymmetric influence of limiters, RF antenna-SOL interactions, or neutral and/or impurity sources (see end of next section). Third, the SOL turbulence could have a structure which is disconnected between these two regions (see Sec. V.E), or due to turbulence near the divertor plate which does not extend to the midplane.

C. Discussion of turbulence velocity

The main result of Sec. IV.C and Figs. 8-10 can be summarized as follows: the time-averaged poloidal velocity of the turbulence is often different in the X-region and midplane view (sometimes even in a different direction), and is usually smaller in the X-region than in the midplane region. The time-averaged radial turbulence velocity is generally smaller than the poloidal velocity, but similar (although uncorrelated) in the two viewing regions. There were also complex velocity variations within both regions for a given shot, and large differences from shot-to-shot and run-to-run. The velocity fluctuations evaluated in Sec. IV.D and shown in Figs. 11-12 were generally uncorrelated between midplane and X-region, except for a low frequency edge oscillation. The turbulence velocity at a single point was nearly constant over 50 ms, except during ELMs, as discussed in Sec. IV.E and illustrated in Fig. 13.

The poloidal turbulence velocity in the SOL is usually assumed to be the sum of the $E_r \times B$ fluid velocity and the phase velocity of the turbulence in the rest frame of the plasma [1,2]. Although the radial electric field was not directly measured in these experiments, in the absence of ICRF-induced radial electric fields (see below) it can be estimated as $\sim 3T_e/L_n \sim 50\text{-}100$ V/cm based on the divertor plate sheath potential profile at the midplane electron temperatures (see Sec. II and Table 2), implying a poloidal $E_r \times B$ flow downward (i.e. negative) of $\sim 1\text{-}2$ km/sec. The diamagnetic velocity should be roughly $V_d = (kT/eB)/L_n \sim 1$ km/sec, either in the positive (upward) direction for electrons or negative (downward) for direction for ions. Thus both of these poloidal velocities are in the measured range of ± 1 km/s, but it is not clear why the direction of the poloidal velocity should reverse from X-region to midplane. It is also not clear whether the phase velocity of the turbulence in the rest frame should in theory be in the electron or ion diamagnetic direction, or even whether this velocity is relevant for the highly turbulent SOL of C-Mod (see also Sec. V.F).

As discussed recently for C-Mod [18] and Tore Supra [20], there are also plasma driven radial, poloidal (i.e. diamagnetic), and parallel flows due to both turbulent transport and neoclassical drifts (see Sec. II), which can be modified by particle sources such as ionization and recycling, or any external sources of toroidal rotation. The net poloidal plasma flows measured using Mach probes in the SOL just above the outer midplane of C-Mod were in the range ≤ 1 km/sec, i.e. similar to the turbulence velocities measured here. However, because of the possible poloidal phase velocity of the turbulence in the rest frame of the plasma, the connection between the turbulence velocities and the plasma flow velocities in this experiment is not yet clear. The radial turbulence velocities of ~ 0.1 km/sec shown in Fig. 10 are similar to those inferred from both particle balance and turbulent transport in [18], but the results of Fig. 10 show no systematic difference between the radial turbulence velocities in the midplane and X-region, suggesting (but not proving) that the radial transport is not much different at these two poloidal angles.

In the ideal MHD limit at low beta (i.e. electrostatic interchange limit) the potential is roughly constant along field lines. Therefore equipotential surfaces in the X-region are given by the field-line mappings of the corresponding equipotential surfaces in the midplane region. Because of magnetic-shear induced ellipticity and tilt, local poloidal and radial turbulence velocities between the two regions can be expected to mix. Furthermore, along elliptical equipotential streamlines, the velocity should be both enhanced and reduced, compared to the circular case at different points along the B field line. These considerations might bear on the scatter evident in Fig. 10.

As noted in Ref. [23], which considers blob-filaments in the low beta ideal MHD limit, if perpendicular viscosity is sufficiently large the whole blob-filament moves as a rigid flux-tube structure. In this limit one would expect that midplane and X-region velocities should be well correlated. There is some evidence for poloidal velocity correlation in Fig. 10, but evidently the large viscosity limit is not strictly applicable to the present dataset. In the highly-collisional limit where local perpendicular 2-D dynamics applies (see Sec. V.D), we expect a localized blob to move primarily in the major radial ($-\nabla B$) direction, which according to Fig. 1 should give comparable radial and poloidal velocities in the X-region. This does not seem to agree with Fig. 10 for 1120224, but is not far off for the other two run days. The local curvature-driven blob velocity can be estimated from Eq. (11) of Ref. [60] as: $V_{\text{blob}} = c_s f_b (\delta_b/R)^{1/2}$, where c_s is the ion sound speed, $f_b = \delta p/p < 1$ is an amplitude factor, and δ_b is the blob radius. Thus for this experiment $V_{\text{blob}} \sim (2 \times 10^6 \text{ cm/sec})(0.3)(1 \text{ cm}/100 \text{ cm})^{1/2} \sim 0.5 \text{ km/sec}$, which is higher than the measured radial turbulence velocities of ~ 0.1 km/sec in Fig. 10.

The most surprising result of Sec. VI.C was that sometimes the direction of the poloidal turbulence velocity was different between these two views, e.g. upward in the X-region and downward in the midplane region in run 1120224. As discussed there, this might be due to the differences in the interaction of the two different viewed flux tubes with the ICRF antennas or, for the run-day without ICRF, due to the fact that some of viewed flux tubes are not toroidally symmetric (see below). It could also be due to a change in the turbulence phase direction in these two regions. Another possibility is that since the GPI views were not perfectly aligned with the local B, then a large parallel

velocity would appear as an artificial poloidal velocity in the GPI. For these two GPI views the misalignment angles were $\leq 1-2^\circ$ (see Sec. III.G), so if the parallel velocities in the SOL were ≤ 20 km/sec [48] (i.e. about half the ion sound speed), then these apparent velocities could be ≤ 0.5 km/sec. Therefore this effect might also contribute to the measured poloidal (or radial) turbulence velocities. Unfortunately, this effect can not be further evaluated without more information about the magnitude of the local parallel flow speed in these two views for these shots.

The only direct cross-correlation observed between the turbulence velocity in the midplane and X-region was associated with a coherent edge mode, as shown in Figs 11 and 12. Thus there is no evidence for $n=0, m=0$ zonal flows in the SOL in this experiment, which perhaps is not surprising since the SOL does not have $m=0$ symmetry. This poloidal flow oscillations seen in the midplane GPI in a previous experiment [16] were only observed at lower density than obtained in the present experiment, and may have been poloidally localized to the outer midplane.

A major uncertainty in these experiments is the effect of the ICRF-induced potentials on the radial electric fields, which has been shown to be present in the C-Mod SOL during ICRF heating [17]. The $E_r \times B$ flows driven by this effect are quite large on flux tubes that magnetically-map to or just in front of active antennas. These potentials are seen to penetrate up to ~ 1 cm into the SOL from the radius of the antenna faces and, because the entire flux tube is affected, are not localized to the toroidal extent of the antennas. The spatial-scale in the radial direction can be sub-cm, typically ~ 0.5 cm. The E_r can be negative (typical) or positive depending on whether the affected field-line is radially inward or outward of the antenna face, and thus can induce flows in either direction. Since at least two of C-Mod's antennas were active during the times of interest during the run-day 1 (1120224) shots and run-day 3 (1120815) shots, this effect will complicate the interpretation of velocities not on the same flux tube for these run-days. We note that the correlation analysis used for the velocity determinations is heavily weighted to the larger size and amplitude fluctuations. Thus these larger (cm-size) fluctuations may not be good "tracers" for the local velocities in the presence of the fine-spatial-scale variations of the ICRF-induced E_r 's. Indeed, image analysis that is sensitive to smaller scale structures show significantly larger velocities and velocity shear in the profiles.

Run-day 2 had no ICRF heating, and as such its analysis is not subject to the concerns mentioned above. However, these shots had an extremely small gap (~ 0.1 cm) between the LCFS and the innermost outboard limiter (mapped to the outboard midplane). This is the "Gap" listed in Table 1. As a result, those SOL field-lines with $\rho > 0.1$ cm may be intercepted by toroidally discrete structures resulting in significantly different connection lengths. Comparisons of the connection lengths within each view at the same ρ show differences of factors of 1.3 to 8 for ρ values > 0.5 cm for these shots. Thus, there is no toroidal symmetry for those ρ regions of the views, and the blob dynamics need not be the same, given those different field-line boundary conditions.

The complex and variable small-scale structure sometimes seen in the 2-D velocity maps like those in Fig. 8 seem to imply localized momentum or particle sources

which can vary significantly from shot-to-shot. We do not have a good explanation for this. In general, it does not seem possible to provide a general theoretical interpretation for the turbulence velocity observations of Sec. IV.C, since there are large variations in the results, large uncertainties in the physics, and several different effects may be occurring at the same time.

D. Correlation of turbulence structure and velocity

The imperfect match between the observed turbulence structure and the magnetic flux tube model of Fig. 14 could in part be due to the interaction between the local turbulence velocity and the turbulence structure. Flow at a uniform velocity should have little or no effect on the turbulence structure, but ExB flow shear, which is known to be present in regions of the SOL in the presence of ICRF-heating (Sect V.C), should affect turbulence when $S=(dV_{\text{pol}}/dr)(L_{\text{rad}}/L_{\text{pol}})\tau \geq 1$, where dV_{pol}/dr is the radial gradient of the poloidal turbulence velocity, L_{rad} and L_{pol} are the turbulence scale lengths, and τ is the turbulence autocorrelation time. Some direct evidence for this turbulence tilting was recently seen in NSTX [27] and Tore Supra [20], and in linear devices such as LAPD [63], in which flow shear can be imposed by external biasing.

The top part of Fig. 15 shows the turbulence structure plotted vs. the poloidal turbulence velocity near the center of the images for run 1220224 (gray areas of Figs. 5 and 8). Each point shows the tilt (or ellipticity) vs. the local poloidal turbulence velocity evaluated at one of the center pixels for each shot. For both the midplane and X-region views there is only a slight increase in the tilt angle with increasing (positive) poloidal velocity, which is also seen in the other runs, and no clear dependence of the ellipticity with poloidal velocity for this or any of the runs. This is consistent with the idea that the turbulence structure should have little or no dependence on the local turbulence velocity itself.

The middle part of Fig. 15 shows the turbulence structure vs. the gradient in the poloidal velocity near the center of the images. Here the poloidal velocity gradient at $\rho=1.0$ cm was found from Fig. 9 as the difference in the zone-averaged poloidal velocities between $\rho=1.25$ cm and $\rho=0.75$ cm, and the tilt and ellipticity were taken for the single pixel at $\rho=1.0$ cm in the central region of the images (with error bars based on the surrounding 8 pixels). There was no clear trend in the tilts, but perhaps a slight increase in the ellipticity with the velocity gradient. However, there is considerable uncertainty in this evaluation of velocity gradients, as can also be seen from the radial profiles in Fig. 9. The largest velocity gradients in Fig. 15 were ~ 1 km/sec/cm for three shots in the midplane view for run 1120224, while for most other cases the velocity gradient was ≤ 0.3 km/sec/cm. A typical normalized shear is $S=(0.3 \text{ km/sec/cm})(1 \text{ cm}/1 \text{ cm})(30 \text{ }\mu\text{sec})\sim 1$, which is close to the level which is supposed to affect the turbulent structure. A large positive shear should stretch an originally circular blob to form a shape at least qualitatively similar to the cross-correlation maps for the midplane data in Fig. 4.

A visual comparison of the 2-D structure maps of Fig. 5 with the 2-D velocity maps of Fig. 8 also suggests some possible correlation between the local turbulence structure and the local velocity fields. For example, in the X-region in shot 1120815021, the largest tilts and ellipticity occur at lower right where the flows are strong and changing direction, and in the midplane the largest tilt is seen at the upper right and the one point at the upper left, which are the regions of strongest flow shear. This motivated the analysis shown at the bottom part of Fig. 15, in which the tilt angle and ellipticity are plotted with respect to the local curl of the vector velocity fields. The local “curlv” on the horizontal axis is the sum of the velocities in the counterclockwise direction at ± 3 pixels (~ 0.3 cm) from the point at which the tilt and ellipticity are evaluated, with all points within ± 0.5 cm of the $\rho=1$ line in maps like those in Figs. 5 and 8 are shown for all shots in run 1120224. There is perhaps a slight trend for the tilt to be correlated with “curlv”, but this is in the opposite direction expected if the turbulence structure rotated in the direction of the local velocity field. No clear trends in such correlations are seen in the other two runs. A more detailed study could be done of the local relationship between the turbulence structure and velocity using both the time-averaged analysis from cross-correlations and the time-resolved blob analysis, as done recently for NSTX [27], but this is beyond the scope of this paper.

E. Additional physics issues

We have discussed in Secs. V.B through D how magnetic flux tube mapping and electric field shear could affect the local turbulence structure. A third possibility is that the major radial stretching of structures observed in the X-region (i.e. a tilt angle $\sim 0^\circ$) might be driven by the local curvature in the X-region, which is predominantly in the R direction due to the dominant toroidal curvature. The flux tube mapping model and Ryutov’s model of blobs [23] are for ideal MHD. However, if we consider the opposite extreme limit of highly resistive MHD, then there is negligible parallel current, so each perpendicular slice of blob propagates independently of the others, all moving in the local $-\nabla B$ direction. In this 2-D limit we would expect the X-region structures to move primarily outward in R, and not to follow the magnetic flux tube mapping model.

The highly resistive limit is defined by a dimensionless collisionality $\Lambda > 1$ [27], where the collisionality parameter $\Lambda = L_{\parallel} \nu_{ei} / (\rho_s \Omega_e)$ may also be written as $\Lambda = (m_e / m_i)^{1/2} \nu_{e*}$, where the dimensionless collisionality $\nu_{e*} = L_{\parallel} / \lambda_{ei}$ (L_{\parallel} is the shortest distance to the divertor plate along a field line, and λ_{ei} is the electron mean free path for collisions with ions). There is quite a range in Λ given the stated uncertainties in n_e and T_e in Table 2, even taking L_{\parallel} as fixed. For L-mode the range is 0.15 to 0.85 and for H-mode the range is 1.1 to 2.2. Blob filaments are expected [6] to become collisionally disconnected from the divertor plate sheaths when Λ exceeds a critical value which is always less than order unity. The critical value is reduced below one by magnetic shear effects that can be estimated from the ellipticity, i.e. the ratio of major to minor radii of the ellipse traced out by field line mapping. Thus, in both the H-mode and L-mode cases the midplane region is at least marginally collisionally disconnected from the sheaths, since ellipticity > 2 is

likely if the field lines are traced past the X region right out to the divertor plates. A separate condition can be given for when the dynamics of two locations on a field line separated by L_{\parallel} become de-correlated due to collisions, i.e. when perpendicular polarization currents become more important than currents. This condition is given by $\Lambda > (\delta_b / \delta_*)^{5/2}$ where δ_b is the blob radius and $\delta_* = \rho_s (L_{\parallel}^2 / \rho_s R)^{1/5}$. For the present dataset $\delta_* \sim 0.15$ to 0.2 cm while $\delta_b \sim 0.5$ to 1.5 cm (e.g. from Fig. 6) so collisional decorrelation of midplane and X-region locations (were they on the same field line) should not occur. This would also be suggested by the fact that strong correlations along the field lines have been observed in other C-Mod experiments [19]. In this limit, the grad-B outward force is averaged along the filament and applied to the filament dynamics as a whole, as opposed to acting locally on a cross-section of the filament.

An additional complication in interpreting the X-region data comes about from a combined effect of the 3-D dynamics and the fact that the He line emission measured by GPI depends on both T_e and n_e . We expect T_e to be communicated rapidly along the field line at v_e (or somewhat slower in conduction-limited regimes), but n_e to be communicated at the much slower speed $\sim c_s$. So if we imagine the plasma is first ejected from the closed flux surfaces near the outer midplane, then the T_e and the electrostatic potential of this perturbation will arrive at the X-region well within a turbulence correlation time, but the density arrives at the X-region only after a parallel ion transit time, which is comparable to the autocorrelation time. Therefore the density fluctuations in the X-region may involve a convolution of parallel propagation and simultaneous radial motion across the local density gradient in the X-region. Since the local density gradient in the X-region is not known from experiment, it is not possible to assess the relative contributions of these two effects.

Finally, the internal dipole electric field pattern of an SOL blob tends to moves the centroid of the blob forward while sweeping backward the exterior plasma (like a swimmer), as illustrated in Fig. 14 of Ref. [6]. So if the blob is moving down a density gradient, it is convecting the lower density exterior plasma on its sides backward into the higher density region. This should appear as a negative cross-correlation, and may explain the negative cross-correlations seen in Fig. 4.

F. Relationship to previous experimental results

As far as we know, there has not previously been a direct comparison of the 2-D structure of SOL turbulence between the two poloidal locations in this experiment. However, as reviewed in the Introduction and [1,2], there have been several previous measurements of a high correlation of tokamak edge turbulence along B field lines [e.g. 3-5], which suggests that the turbulence should be similar at different poloidal angles. On the other hand, there also have been previous observations poloidal asymmetries of the edge turbulence in circular tokamaks [61,62], which implies that the turbulence can vary along B field lines. Therefore it is not too surprising that the SOL turbulence

structure and velocity in the present experiment were in some cases significantly different at these two different poloidal locations in C-Mod.

As noted in the Sec. I, the most closely related recent results in this area were from the Tore Supra [20] and EAST [20,21] tokamaks. Probe measurements at the top of Tore Supra [20] were consistent with a magnetic flux tube mapping model, and the first results from a dual-GPI diagnostic on EAST showed significant differences in the turbulence velocity and structure above and below the outer midplane. These results are qualitatively consistent with the present results in that the turbulence was different at two poloidal locations, but there is not enough information for quantitative comparisons.

The initial results from the X-region GPI view in C-Mod [12] showed similar turbulence structure to that described here in Sec. IV.B, although the earlier data were for double-null, upper single null, and limited configurations taken using D₂ GPI puffs. The large variation of the tilt angle within the X-region view in [12] was not seen in the present results, perhaps due to the different magnetic structure or the different GPI gas. Also, in [12] the radial turbulence velocities seemed to be $\sim 3\times$ faster than those previously seen at the outer midplane, although no simultaneous comparison was available then, whereas the present results in Fig. 10 show a similar radial velocity in both views.

The absence of cross-correlation between the turbulent structures and velocities in the midplane and X-point camera images (Appendix and Fig. 12) suggests that turbulence in these two regions develops independently, probably because these regions are on different B field line. However, there is other striking experimental evidence that those structures form filaments which extend along a single magnetic field from the outboard midplane to the X-point region [19]. Using a specially programmed magnetic field geometry which allowed for direct connection along a B field line between the outer midplane GPI and an X-point region Langmuir probe, recent measurements revealed that the turbulent fluctuations are highly correlated along the magnetic field, with maximum correlation amplitudes of $>90\%$. High correlations were even observed past the X-point region to the divertor plates. However, those filaments were found to have non-zero k_{\parallel} significantly larger than expected for resistive ballooning, which indicates the importance of parallel response between the X-point and midplane region. This high two-point correlation along B does not necessarily imply that the 2-D shape of the turbulence or the turbulence velocity is the same in both regions, and unfortunately there was no X-region GPI camera data for that experiment to check the 2-D structure comparison.

G. Conclusions and suggestions for further research

This paper described 2-D imaging of plasma turbulence in the scrape-off layer of the Alcator C-Mod tokamak at two different poloidal locations, one near the outer midplane and the other near the divertor X-point region. These images were made simultaneously with radial vs. poloidal resolution using two gas puff imaging diagnostics. The main conclusions of the paper were as follows:

- 1) The basic turbulence characteristics were similar between the midplane and X-point region, as described in Sec. IV.A. The SOL plasma is strongly turbulent in both regions, as discussed in Sec. V.A.
- 2) The tilt angle of the turbulent structures in the SOL was significantly different in the midplane and X-regions, as described in Sec. IV.B. This was partially (but not perfectly) consistent with a simple magnetic flux tube model, as discussed in Sec. V.B.
- 3) The poloidal turbulence velocity was sometimes significantly different between the midplane and X-regions, while the radial turbulence velocities had similar magnitudes in the midplane and X-region, as discussed in Sec. IV.C. There were several factors which could affect these velocities, as discussed in Sec. V.C.
- 4) The turbulence structure was not significantly correlated with the turbulence velocity, but perhaps slightly correlated with the local velocity gradient, as described in Sec. IV.D. The possible effect of ExB shearing and parallel disconnection on the structures was discussed in Secs. V.D and E.

In addition to these main conclusions, some new and unexplained results were: the turbulence structure in the midplane view was systematically tilted with respect to the local flux surfaces (Fig. 7); the turbulence velocity sometimes had variable small-scale features within each view (Fig. 8); the turbulence could move in different poloidal directions in the two views (Figs. 9 and 10); and there was sometimes a coherent oscillation in the turbulence velocity common to both views (Figs. 11 and 12).

There were also several issues which were left unresolved in this paper. These experiments should be repeated without the complicating feature of ICRF-heating and the large SOL radial electric field typically observed with the ICRF in C-Mod [17]. Furthermore, for shots without the ICRF it would be useful to have cases in which the outer “gaps” were large enough so that the toroidal symmetry is better preserved in the analyzed SOL regions. The present results need to be reconciled with the high parallel correlation observed for SOL turbulence along B field lines in other C-Mod experiments [4,19]. Also, in general the turbulence velocities derived from cross-correlation analysis used here do not necessarily agree with the turbulence phase velocities derived from frequency vs. wavenumber analysis [17], for reasons which are not yet understood.

There are many directions for future research in this area. The various uncertainties and limitations of the GPI diagnostic and data analysis described in Sec. III.G could be reduced with more hardware and software improvements. Additional gas puff imaging measurements could be made at other poloidal and toroidal angles to clarify the full 3-D edge turbulence structure, and direct comparisons with other edge turbulence and/or flow diagnostics would be very valuable. More detailed modeling of the GPI diagnostic resolution and sensitivity could be done using a neutral code such as DEGAS 2, given additional edge temperature and density profile data and 3-D imaging of the GPI gas cloud. Data analysis methods should be developed to quantify the complex 2-D

structures and motions observed, including statistical uncertainties. Effects of 3-D magnetic structures and non-axisymmetric limiter and ICRF antenna perturbations should be clarified. Finally, 3-D turbulence simulations need to be done to understand these results and predict the effects of this turbulence on SOL transport in future tokamaks.

Acknowledgments: We thank D.A. D'Ippolito, E. Feibush, T. Munsat and D.A. Russell, B.D. Scott, M.V. Umansky, and G.S. Xu for their contributions and/or comments on this paper. S.J. Zweben would like to thank the Alcator C-Mod group for their long-term support for this research, which was funded in part by US DOE Contracts DE-AC02-09CH11466 and DE-FC02-99ER5412.

Appendix: Magnetic field line mapping

At the left of Fig. 16 is a toroidal vs. z -coordinate map of magnetic field lines starting from the vertical center of the midplane view at $\rho=1$ cm, i.e. at $z=-3$ cm and toroidal angle = 0. None of these B field lines intersect the X-region view, the projection of which onto $R=R_{\text{view center}}$ plane which is indicated by the black box. This is not surprising since these GPI views were not designed to be on the same field line. Other field lines started from $\rho=2$ cm and at $\rho=0.2$ cm (from $z=-6$ cm and $\phi=0$, the lowest point in the midplane view) also do not intersect the X-region view, with the closest approach being ~ 11 cm. This suggests there should be little or no cross-correlation between turbulence in these two views, based on the flux tube mapping model.

At the right of this figure is an analysis of the actual cross-correlation of the turbulence between the midplane and X-region views for all shots in Table 1. This was done by correlating every third pixel in the midplane region with all pixels in the X-region using time delays of up to ± 2 frames ($\pm 4.2 \mu\text{s}$), i.e. in the time delay range of turbulence cross-correlations along a B field line [19]. The average cross-correlations are shown by the triangles, and the maximum cross-correlations are shown by the circles. These data are grouped according to run day, and the random level of cross-correlation is evaluated by using the midplane data from one shot and the X-region data from another shot (1120712026 and 027), and *vice versa*, as shown at the right. The result is that there was no significant cross-correlation between the turbulence in the midplane and X-region views, except for one shot (1120712026). The higher cross-correlation for 1120712026 appears to be due to a macroscopic global fluctuation that is apparent on both GPI signals as well as a D_α emission monitor viewing neither of the GPI regions. This is generally consistent with the model that the turbulence follows the magnetic flux tubes.

Table 1: Shot List

Shot	Time (sec)	I(MA)	B(T)	n (m ⁻³)	RF(MW)	Gap*(cm)	Discharge type
Run day 1:							
1120224009	0.701-0.716	0.9	4.6	1.1x10 ²⁰	2.3	1.3	L-mode
1120224015	0.810-0.814	1.0	6.0	1.3x10 ²⁰	3.7	1.1	L-mode
1120224022	1.044-1.048	1.0	5.2	1.0x10 ²⁰	2.6	1.2	L-mode
1120224023	1.113-1.116	1.0	5.2	1.4x10 ²⁰	3.0	1.3	ELM-free H-mode
1120224024	1.130-1.135	1.0	5.2	1.7x10 ²⁰	2.8	1.5	ELM-free H-mode
1120224027	1.144-1.148	0.9	4.6	1.3x10 ²⁰	3.0	1.4	L-mode
Run day 2:							
1120712026	1.440-1.444	0.73	4.2	3.5x10 ²⁰	0	0.2	Ohmic H-mode
1120712027	1.440-1.444	0.73	4.2	3.6x10 ²⁰	0	0.1	Ohmic H-mode
1120712028	1.440-1.443	0.73	5.0	2.6x10 ²⁰	0	0.1	Ohmic H-mode
1120712029	1.440-1.443	0.73	5.0	2.2x10 ²⁰	0	0.1	Ohmic H-mode
Run day 3:							
1120815018	1.270-1.274	0.90	5.6	2.5 x10 ²⁰	2.9	1.4	ELMy H-mode
1120815021	1.190-1.193	0.91	5.6	2.0 x10 ²⁰	2.0	1.4	ELMy H-mode
1120815030	1.260-1.264	0.91	5.6	1.9 x10 ²⁰	2.6	1.5	ELMy H-mode
1120815034	1.150-1.153	0.91	5.6	2.0 x10 ²⁰	3.1	1.7	ELMy H-mode

* outer gap distance between outer midplane separatrix and innermost outer limiter

Table 2: Typical SOL parameters

parameter	1120224	1120815
regime	L-mode	H-mode
ρ at midplane (cm)	0.5±0.5	0.5±0.5
n_e (10 ¹⁹ m ⁻³)	3.1±1.1	4.9±0.6
T_e (eV)	21±5	18±2
L_n (cm)	1.1	1.2
L_{Te} (cm)	0.6	0.5
$L_{ , min}$ (m)	~ 4	~ 8
ρ_s (cm)	~10 ⁻²	~10 ⁻²
$v_{e*}(m_e/m_i)^{1/2}$	0.4	1.6
β	~3x10 ⁻⁵	~3x10 ⁻⁵

References

- [1] S.J. Zweben, J.A. Boedo, O. Grulke, C. Hidalgo, B. LaBombard, R.J. Maqueda, P. Scarin and J.L. Terry, *Plasma Phys. Cont. Fusion* **49**, S1 (2007)
- [2] J.A. Boedo, *J. Nucl. Mat.* **390-391**, 29 (2009)
- [3] H. Thomsen, M. Endler, J. Bleul, A.V. Chankin, S.K. Erements, G.F. Matthews and Contributors to the EFDA-JET work programme, *Phys. Plasmas* **9**, 1233 (2002)
- [4] O. Grulke, J.L. Terry, B. LaBombard, S.J. Zweben, *Phys. Plasmas* **13**, 012306 (2006)
- [5] R. Maqueda, D.P. Stotler and the NSTX Team, *Nucl. Fusion* **50**, 075002 (2010)
- [6] D. D'Ippolito, J.R. Myra, S.J. Zweben et al, *Phys. Plasmas* **18**, 060501 (2011)
- [7] J.R. Angus, S.I. Krasheninnikov, M. Umansky, *Phys. Plasmas* **19**, 0823132 (2012)
- [8] J. L. Terry, S.J. Zweben, K. Hallatschek, B. LaBombard, R.J. Maqueda, B. Bai, C.J. Boswell, M. Greenwald, D. Kopon, W.M. Nevins, C.S. Pitcher, B.N. Rogers, D.P. Stotler, and X.Q. Xu, *Phys. Plasmas*, **10**, 1739 (2003)
- [9] I. Garcia-Cortes, C. Hidalgo, J.R. Martin-Solis, S. Ali-Arshad, S. Clement, S.J. Davies, J. Lingertat, A. Loarte, G.F. Matthews and R.D. Monk, *Plasma Phys. Cont. Fusion* **38**, 2051 (1996)
- [10] R.A. Moyer, R. Lehmer, J.A. Boedo, J.G. Watkins, X. Xu, J.R. Myra, R. Cohen, D.A. D'Ippolito, T.W. Petrie, M.J. Schaffer, *J. Nucl. Mat.* **266-269**, 1145 (1999)
- [11] G. Y. Antar, G. Counsell, J.-W. Ahn, Y. Yang, M. Price, A. Tabasso, and A. Kirk, *Phys. Plasmas* **12**, 032506 (2005)
- [12] J.L. Terry, S.J. Zweben, M.V. Umansky, I. Cziegler, O. Grulke, B. LaBombard, D.P. Stotler, *J. Nucl. Mat.* **390-391**, 339 (2009)
- [13] Y. Xu, I. Shesterikov, M. Van Schoor, M. Vergote, R.R. Weynants, A. Kramer-Flecken, S. Zoletnik, S. Soldatov, D. Reiser, K. Hallatschek, C. Hidalgo and the TEXTOR Team, *Plasma Phys. Cont. Fusion* **53**, 09015 (2011)
- [14] J. C. Hillesheim, W. A. Peebles, T. A. Carter, L. Schmitz, and T. L. Rhodes, *Phys. Plasmas* **19**, 022301 (2012)
- [15] A. D. Liu, T. Lan, C. X. Yu, H. L. Zhao, L. W. Yan, W. Y. Hong, J. Q. Dong, K. J. Zhao, J. Qian, J. Cheng, X. R. Duan, and Y. Liu, *Phys. Rev. Lett.* **103**, 095002 (2009)
- [16] S.J. Zweben, J.L. Terry, M. Agostini, R. Hager, J.W. Hughes, J.R. Myra, D.C. Pace

- and the Alcator C-Mod Group, *Plasma Phys. Cont. Fusion* **54**, 025008 (2012)
- [17] I. Cziegler, J.L. Terry, S.J. Wukitch, M.L. Garrett, C. Lau, Y. Lin, *Plasma Phys. Cont. Fusion* **54**, 105019 (2012)
- [18] N. Smick, B. LaBombard, and I.H. Hutchinson, *Nucl. Fusion* **53**, 023001 (2013)
- [19] O. Grulke et al, private communication (2013)
- [20] N. Fedorczak, P. Manz, S.C. Thakur, M. Xu, G.R. Tynan, G. S. Xu, and S. C. Liu, *Phys. Plasmas* **19**, 122302 (2012)
- [21] S.C. Liu, L.M. Shao, S.J. Zweben, G.S. Xu, H. Y. Guo, B. Cao, H.Q. Wang, L. Wang, N. Yan, S.B. Xia, W. Zhang, R. Chen, L. Chen, S.Y. Ding, H. Xiong, Y. Zhao, B.N. Wan, X.Z. Gong, and X. Gao, *Rev. Sci. Inst.* **83**, 123506 (2012)
- [22] D. Farina, R. Pozzoli, and D. Ryutov, *Plasma Phys. Controlled Fusion* **35**, 1271 (1993)
- [23] D.D. Ryutov, *Phys. Plasmas* **13**, 112307 (2006)
- [24] J.R. Angus, M.V. Umansky, and S.I. Krasheninnikov, *Phys. Rev. Lett* **108**, 215002 (2012)
- [25] E. Havlickova, W. Fundamenski, V. Naulin, A.H. Nielsen, R. Zagorski, J. Seidl, J. Horacek, *Plasma Phys. Cont. Fusion* **53**, 065004 (2011)
- [26] G.Q. Yu, S.I. Krasheninnikov, P.N. Guzdar, *Phys. Plasmas* **13**, 042508 (2006)
- [27] J.R. Myra, W.M. Davis, D.A. D'Ippolito, B. LaBombard, D.A. Russell, J.L. Terry, and S.J. Zweben “Edge sheared flows and the dynamics of blob-filaments”, presented at the 24th IAEA Fusion Energy Conference, San Diego, USA, October 8 - 13, 2012, paper IAEA-CN-197/TH/P4-23.
- [28] K. Bodi, S.I. Krasheninnikov, A.I. Smolyakov, *Phys. Plasmas* **15**, 102304 (2008)
- [29] D.A. Baver, J.R. Myra, M.V. Umansky, *Computer Physics Communications* **182** 1610 (2011)
- [30] A. Masetto, F.D. Halpern, S. Jolliet, and P. Ricci, *Phys. Plasmas* **19**, 112103 (2012)
- [31] B.D. Scott, *Plasma Phys. Cont. Fusion* **49**, S25 (2007)
- [32] R.H. Cohen, B. LaBombard, D. D. Ryutov, J. L. Terry, M. V. Umansky, X. Q. Xu, and S. Zweben, *Nucl. Fusion* **47**, 612 (2007).
- [33] S. J. Zweben, B. D. Scott, J. L. Terry, B. LaBombard, J. W. Hughes, and D. P.

Stotler, Phys. Plasmas **16**, 082505 (2009)

[34] P. Ricci and B.N. Rogers, Phys. Plasmas **20**, 010702 (2013)

[35] B.I. Cohen, M.V. Umansky, W.M. Nevins, M.A. Makowski, J.A. Boedo, G. McKee, Z. Yan, D. Rudakov, R. Groeber and the DIII-D Collaboration, submitted to Phys. Plasmas (2012)

[36] P. Stangeby, “The Plasma Boundary of Magnetic Fusion Devices”, Plasma Physics Series (IOP, Bristol, 2000) chapter 15 & 17.

[37] B. LaBombard, D. Brunner, O.E. Garcia, M. Greenwald, J.W. Hughes, R. Kube, J.L. Terry, S. Zweben, Bull Am Phys Soc *57*, paper BO7.00014 (2012)

[38] A. N Simakov, P.J. Catto, B. LaBombard, and A.H. Glasser, Plasma Phys. Control. Fusion **50**, 105010 (2008).

[39] M. Landreman and D. Ernst, Plasma Phys. Control. Fusion **54**, 115006 (2012)

[40] S.J. Zweben, R.J. Maqueda, D.P. Stotler, A. Keesee, J. Boedo, C.E. Bush, S.M. Kaye, B. LeBlanc, J.L. Lowrance, V.J. Mastrocola, R. Maingi, N. Nishino, G. Renda, D.W. Swain, J.B. Wilgen and the NSTX Team, Nucl. Fusion **44**, 134 (2004)

[41] M. Agostini, R. Cavazzana, P. Scarin, and G. Serianni, Rev. Sci. Instrum. **77**, 10E513 (2006).

[42] Y. Nakashima, N. Nishino, Y. Higashizono, H. Kawano, S. Kobayashi, M. Shoji, Y. Kubota, M. Yoshikawa, M. K. Islam, Y. Mishima, D. Mimura, and T. Cho, J. Nucl. Mater. **363-365**, 616 (2007).

[43] N. Nishino, T. Mizuuchi, Z. Feng, S. Kobayashi, K. Nagasaki, H. Okada, Y. Torii, K. Kondo, and F. Sano, J. Nucl. Mater. **363-365**, 628 (2007).

[44] I. Shesterikov, Y. Xu, C. Hidalgo, M. Berte, P. Dumortier, M. Van Schoor, M. Vergote, G. Van Oost, and TEXTOR Team, Nucl. Fusion **52**, 042004 (2012)

[45] D.P. Stotler, B. LaBombard, J.L. Terry, S.J. Zweben, Journal of Nuclear Materials **313-316** 1066 (2003)

[46] D.P. Stotler, J. Boedo, B. LeBlanc, R.J. Maqueda, S.J. Zweben, J. Nucl. Mat **363-365**, 686 (2007)

[47] B. Cao, D.P. Stotler, S.J. Zweben, M. Bell, A. Diallo, B. LeBlanc, “Comparison of gas puff imaging data in NSTX with the DEGAS 2 simulation” to be published in Fusion Science and Technology (2013)

[48] D.C. Pace, private communication (2013)

- [49] T. Golfinopoulos, private communication (2013)
- [50] J.W. Hughes, P.B. Snyder, J.R. Walk, E.M. Davis, A. Diallo, B. LaBombard, S.G. Baek, R.M. Churchill, M. Greenwald, R.J. Groebner, A.E. Hubbard, B. Lipschultz, E.S. Marmor, T. Osborne, M.L. Reinke, J.E. Rice, C. Theiler, J. Terry, A.E. White, D.G. Whyte, S. Wolfe and X.Q. Xu, *Nucl. Fusion* **53**, 043016 (2013)
- [51] J.L. Terry, B. LaBombard, B. Lipschultz, M.J. Greenwald, J.E. Rice, and S.J. Zweben, *Fusion Sci. Tech.* **51**, 342 (2007)
- [52] <http://w3.pppl.gov/~szweben/CMod2012both/CMod2012both.html>
- [53] S.J. Zweben, R.J. Maqueda, A.L. Roquemore, C.E. Bush, R. Kaita, R.J. Marsala, Y. Raitses, R.H. Cohen and D.D. Ryutov, *Plasma Phys. Cont. Fusion* **51**, 105012 (2009)
- [54] M. Agostini, R. Cavazzana, P. Scarin, G. Serianni, Y. Yagi, H. Koguchi, S. Kiyama, H. Sakakita and Y Hirano, *Plasma Phys. Cont. Fusion* **50**, 095004 (2008)
- [55] T. Munsat and S.J. Zweben, *Rev. Sci. Inst.* **77**, 103501 (2006)
- [56] B. Tal, A. Bencze, S. Zoletnik, G. Veres, and G. Por, *Phys. Plasmas* **18**, 122304 (2011)
- [57] S. Zoletnik, L. Bardoczi, A. Kramer-Flecken, Y. Xu, I. Shesterikov, S. Soldatov, G. Anda, D Dunai, G Petravich and the TEXTOR Team, *Plasma Phys. Cont. Fusion* **54**, 065007 (2012)
- [58] M. Agostini, private communication (2013)
- [59] D.A. Russell, D.A. D'Ippolito, J.R. Myra, B. LaBombard, J. L. Terry, and S. J. Zweben, *Phys. Plasmas* **19**, 082311 (2012)
- [60] J.R. Myra, D.A. D'Ippolito, D.P. Stotler, S.J. Zweben, B.P. LeBlanc, J.E. Menard, R.J. Maqueda, and J. Boedo, *Phys. Plasmas* **13**, 092509 (2006)
- [61] D.L. Brower, W.A. Peebles, N.C. Luhmann, Jr, *Nucl. Fusion* **27**, 2055 (1987)
- [62] C. Fenzi, X. Garbet, A. Truc, H. Capes, P. Devynck, F. Gervais, P. Hennequin, C. Laviro, and A. Quemeneur, *Nucl. Fusion* **40**, 1621 (2000)
- [63] T. Carter and J.E. Maggs, *Phys. Plasmas* **16**, 012304 (2009)

Figure Captions

1) Typical C-Mod plasma cross-section showing the locations of the midplane and X-region GPI views and nearby flux surfaces (#1120224022). Each GPI view is 5.9 cm x 5.9 cm and oriented in the local radial vs. poloidal (i.e. bi-normal) direction. The black shapes show the poloidal variation of an assumed circular magnetic flux tube at the outer midplane. At the right is a 3-D visualization of a magnetic flux tube along the 1.7 meters between the midplane view and the X-region view.

2) Typical images of a single frame from the X-region camera (left) and the midplane camera (right), taken at the same time. The data were all normalized by the time-averaged of the images over 4 msec, and displayed in a false-color scale from 0.5 (black) to 1.5 (white), with low-signal-level pixels set to black. The separatrix at $\rho=0$ cm and SOL flux surfaces at $\rho=1$ cm and 2 cm are shown by solid and dashed lines, respectively, and the limiter shadow is shown by the black line in the midplane view. The turbulence structures tend to be elongated in the major radial direction in the X-region region and more circular in the midplane region.

3) Comparison of basic turbulence characteristics in the midplane and X-region GPI views for three typical shots, one from each of the run days of Table 1. At the top are radial profiles of the relative GPI fluctuation levels (standard deviation/mean), in the middle are the autocorrelation times (FWHM), and at the bottom are the frequency spectra (FFT amplitude) averaged over regions near the center of the images at $\rho=1$ cm. The basic turbulence characteristics were similar in the outer midplane and X-region GPI data.

4) Typical 2-D spatial cross-correlation functions for the X-region (left) and midplane view (right), calculated from the central points marked with an "x", and averaged over 3 msec in time. This color scale has red near 1.0 (i.e. perfect cross-correlation), green near 0, blue near -0.5, and black at -1.0. The size and shapes of the correlation functions are roughly the same size in both regions, but they are tilted at different angles with respect to the (R,z) plane.

5) Typical shapes of the cross-correlations in the X-region (left) and midplane (right) for four typical shots. These maps are drawn for the same regions as Figs. 2 and 4 and oriented in the same direction. The shapes and tilt direction of the black ellipses are defined at a spatial cross-correlation coefficient of 0.7, but their size is reduced by a factor of 3 so they do not overlap. The gray areas show the central regions used for database analysis.

6) Comparison between the correlation lengths in the midplane and X-region for all shots of Table 1, sorted according to run day. These lengths are based on maps like Figs. 4 and 5, but using only pixels near at the center of the images (gray regions in Fig. 5). At the

left are the maximum correlation lengths in the 2-D image plane, in the middle are the minimum correlation widths, and at the right is the area of these correlation structures. If these turbulence followed magnetic flux tubes the areas in the X-region would be ~ 0.8 that in the midplane due to the $1/R$ toroidal field, indicated by the line at the right.

7) Parameterization of the shapes of the 2-D turbulence structures for the central regions used for Fig. 6, but now plotting separately each pixel for each run day. The tilt angle plotted on the vertical axis of Fig. 7 is the angle at which the cross-correlation function had its largest width, as measured counter-clockwise from the horizontal major radius direction. The ellipticity plotted on the horizontal axis is the ratio of this largest width to the width perpendicular to this direction (nearly the same as the minimum width). The solid symbols in Fig. 7 were based on cross-correlation analysis, as for Fig. 6, while the open symbols were based on a blob structure analysis for each shot (see Sec. III.E). The local tilt of the magnetic flux surfaces are shown by the horizontal bars in each case.

8) Typical 2-D maps of the time-averaged velocity vectors for the X-region (left) and the midplane (right) for four shots. The orientation is the same as for Fig. 5, and the images are overlaid with the separatrix (solid line) and flux surfaces at 0.5 cm radial intervals (dashed lines). Velocity vectors are shown for every third pixel for the regions with good signal levels. These vectors are drawn with a maximum velocity for each shot specified in the upper left corner of each image, and scaled according to this velocity for each image separately. These velocity maps show rather complex flow patterns which can vary significantly within and between these two GPI views. The gray regions near $\rho=1$ cm are used for database analysis.

9) Comparisons between radial profiles of the poloidal velocities V_{pol} between the midplane and X-regions, found by averaging over radial zones of width 0.5 cm in maps like those of Fig. 8. Each point in Fig. 9 represents one shot and has an error bars showing the standard deviations of V_{pol} over the ~ 20 -30 pixels in that radial zone for that shot (note the different vertical scales). The V_{pol} profiles of 1120224 are significantly different between midplane and X-region views (i.e. largely outside the mutual error bars), with a dominantly positive (electron diamagnetic direction) turbulence velocity in the X-region view and a dominantly electron diamagnetic velocity in the midplane view.

10) The same radial profile data as in Fig. 9, but now plotting the midplane velocity vs. the X-region velocity for all shots and radii. At the left are the poloidal velocities and at the right are the radial velocities, all sorted in color by run day as for Fig. 6. The radial velocities are almost all positive (outward radially), and significantly smaller than the poloidal velocities (note the change in velocity scales). The few negative radial velocities are for points near the separatrix.

11) An example of a clear oscillation in the poloidal velocity δV_{pol} in both the midplane and X-region GPI views, also correlated with a $D\alpha$ light fluctuation (upper left). In this case (1120224024) the oscillation is at 2.3 kHz, which is also seen in the spectra of the GPI $D\alpha$ signals shown at the right. A similar but weaker edge oscillation in the frequency range ~ 2 -5 kHz occurred for many of the shots in the run of 1220224.

12) Analysis of the cross-correlation of the δV_{pol} fluctuations between the two GPI views as a function of radius for all shots in Table 1. The δV_{pol} fluctuations in each view were averaged over flux surfaces of 0.5 cm width for each shot. The vertical axis is the maximum value of the cross-correlation function, searching over a time lag of up to $\pm 800 \mu\text{sec}$, and averaging over the analysis time of $\sim 3\text{-}5 \text{ msec}$. The two shots with maximum cross-correlation coefficients above 0.3 were both H-mode cases with the low frequency edge mode discussed above (i.e. 1120224024).

13) The longer-time evolution of the turbulence tilt angle (left) and poloidal velocity (right) for three typical shots for 10 successive 5 msec segments time periods. These analyses were done using only one central pixel at $\rho=1 \text{ cm}$, such as shown by the “x” in Fig. 4. The time axes are relative, and the times used for the shorter analysis times in Table 1 are shown as boxes just above the horizontal axis. For two of these shots there was no significant longer-term time dependence, but for the third shot (1120815021) the presence of ELMs sometimes transiently increased the tilt angle.

14) Comparison of the measured turbulence structure in both GPI views with the magnetic flux tube model. The experimental data is the same as in Fig. 5 but here for a single shot for the central regions near $\rho=1 \text{ cm}$, analyzed either using cross-correlations (triangles) or blob analysis (circles). The colored ellipses show the mapping of flux tubes for this shot for an assumed radial location $\rho=1$, starting from the midplane (where they are fit to the data) and ending where they reach the X-region region (bottom). The shape and tilt of these ellipses reflect their location on this plot.

15) At the top is the turbulence structure *vs.* the poloidal turbulence velocity for pixels near the center of the images for run 1220224. Each point shows the tilt (left) or ellipticity (right) evaluated at one of the central pixels for each shot. At the bottom is the turbulence structure *vs.* the gradient in the poloidal velocity at $\rho=1.0 \text{ cm}$, found from Fig. 9 as the difference in the zone-averaged poloidal velocities between $\rho=1.25 \text{ cm}$ and $\rho=0.75 \text{ cm}$. The tilt and ellipticity at the bottom were taken for the single pixel at the central region of the images (with error bars based on the surrounding 8 pixels).

16) At the left is a map showing the toroidal *vs.* vertical trajectories of magnetic field lines at starting $\rho=1 \text{ cm}$ in the midplane viewing region for all shots in this experiment, with the location of the X-region GPI view indicated by the black box. The plot on the right is the measured average and maximum cross-correlation coefficient of the turbulence between the two views for each shot, and between two different shots (right). Except for one shot (1120712026) there is little or no significant cross-correlation, as expected from the mapping.

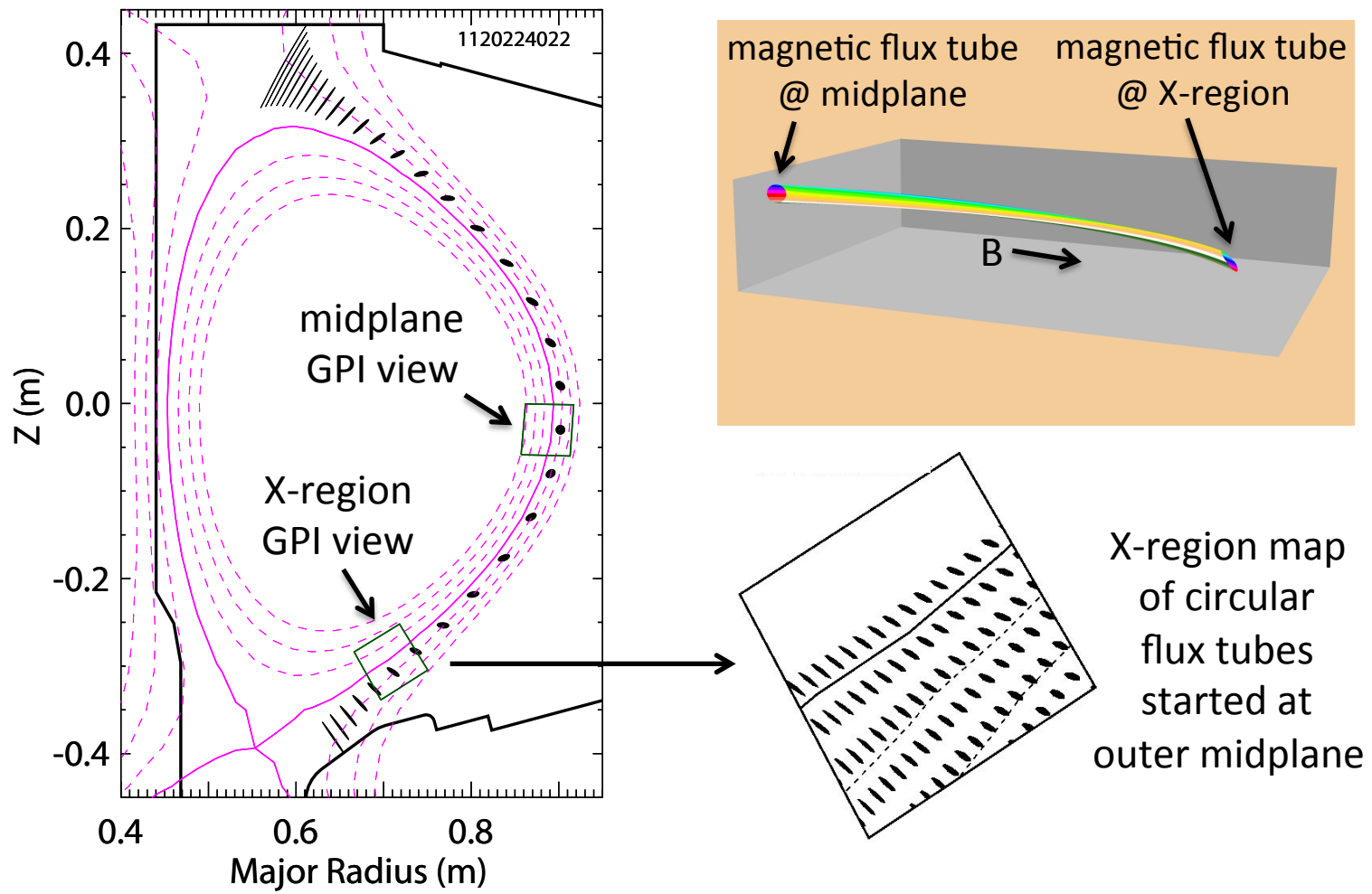


Fig. 1

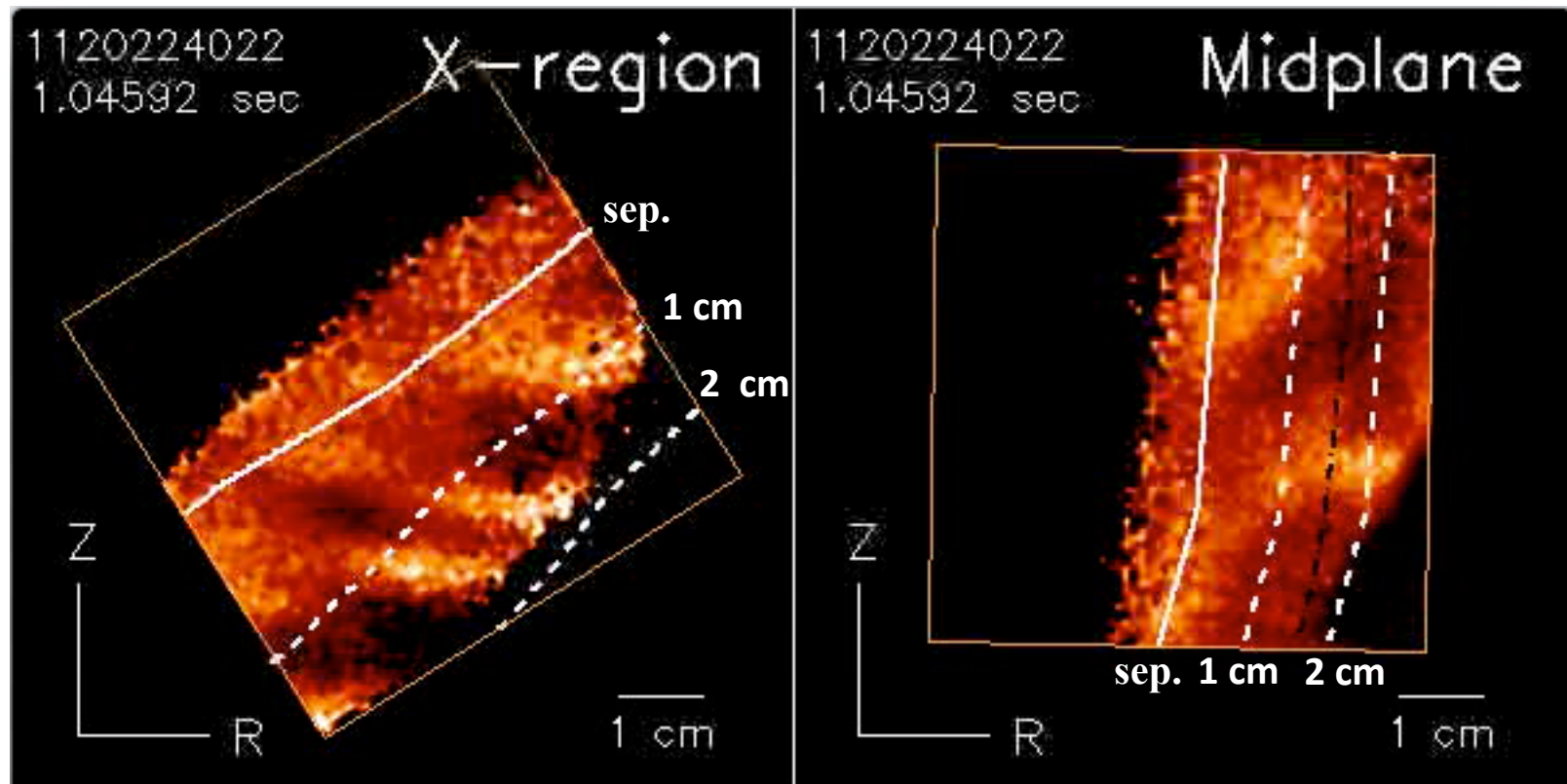


Fig. 2

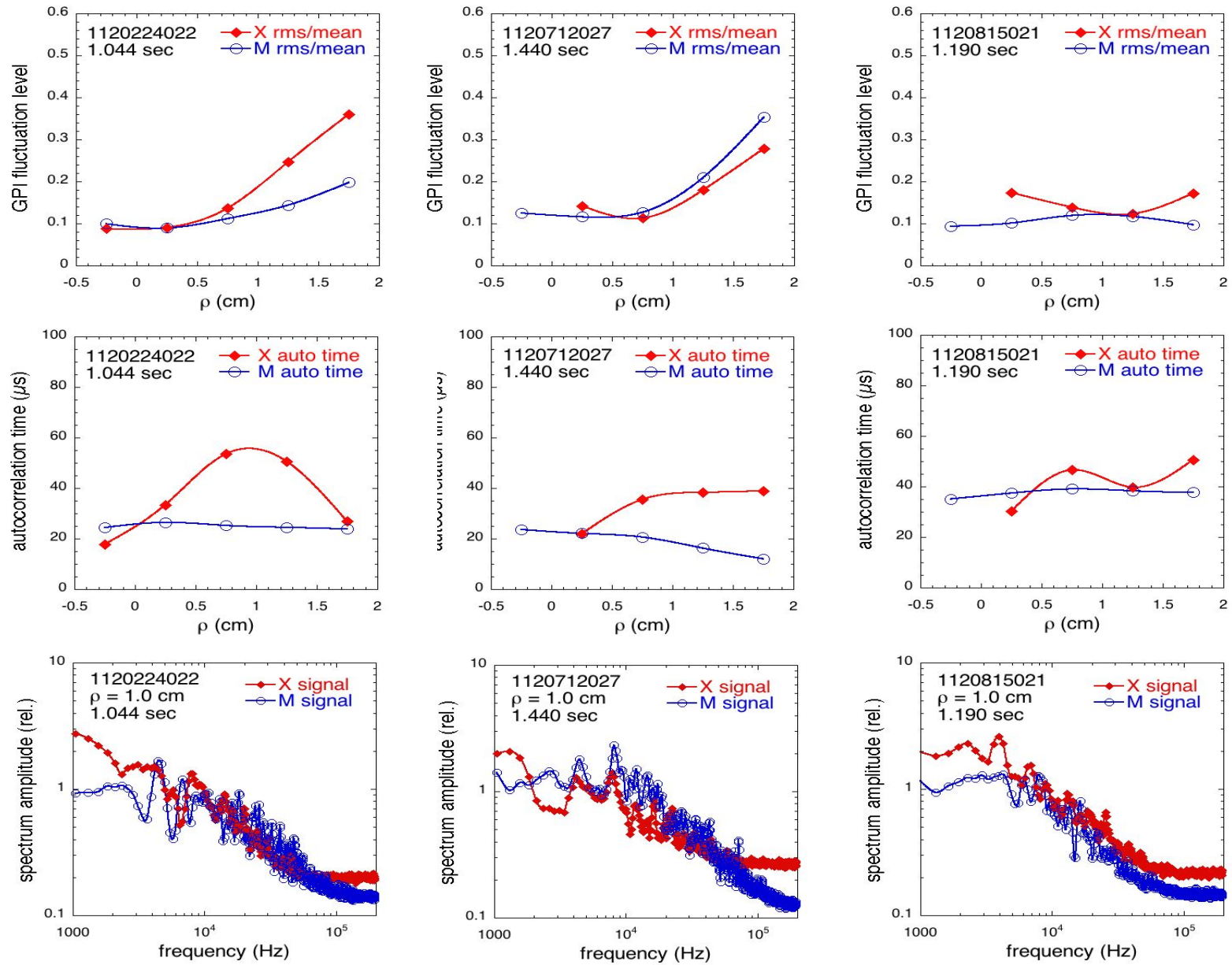


Fig. 3

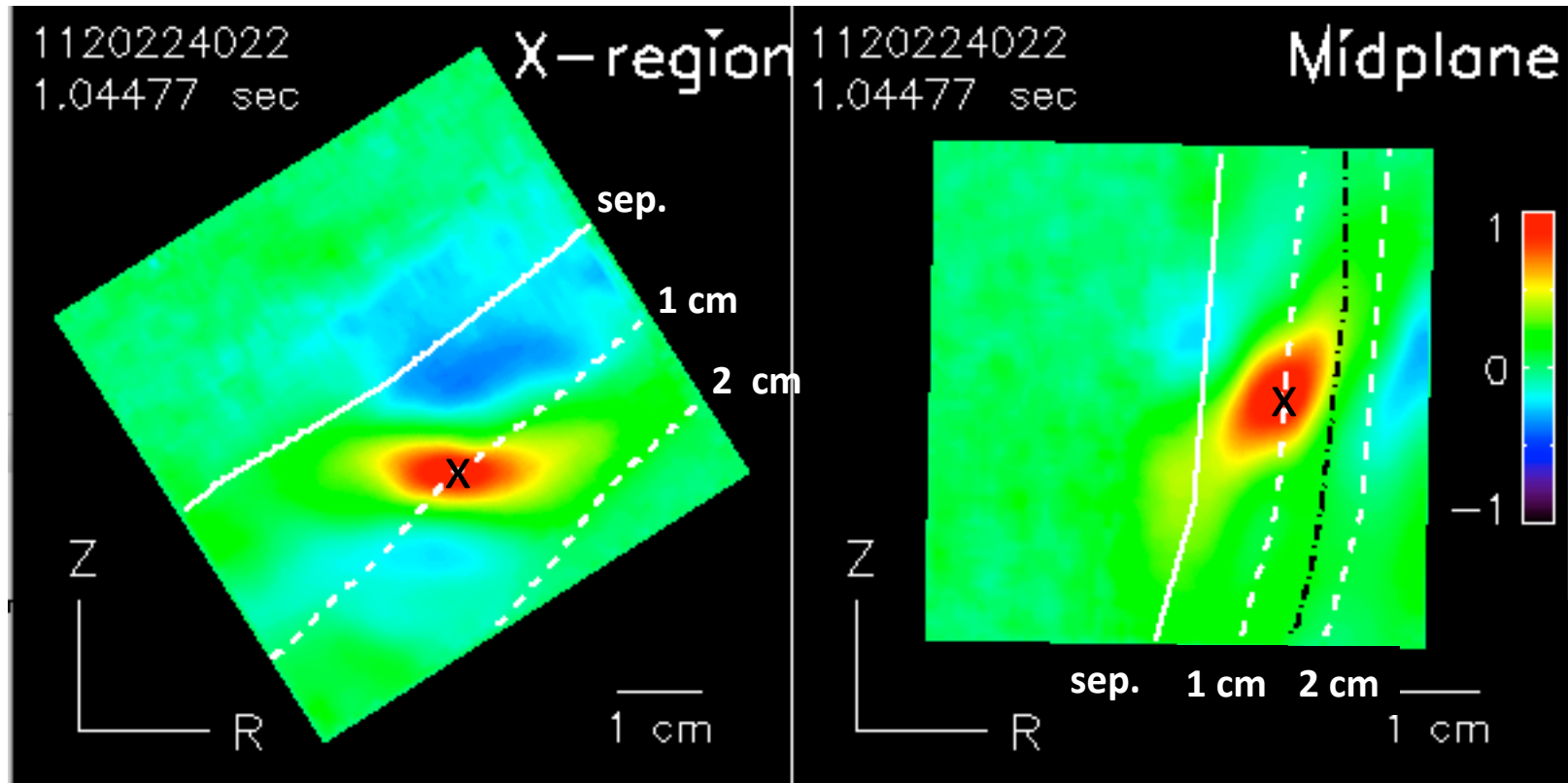


Fig. 4

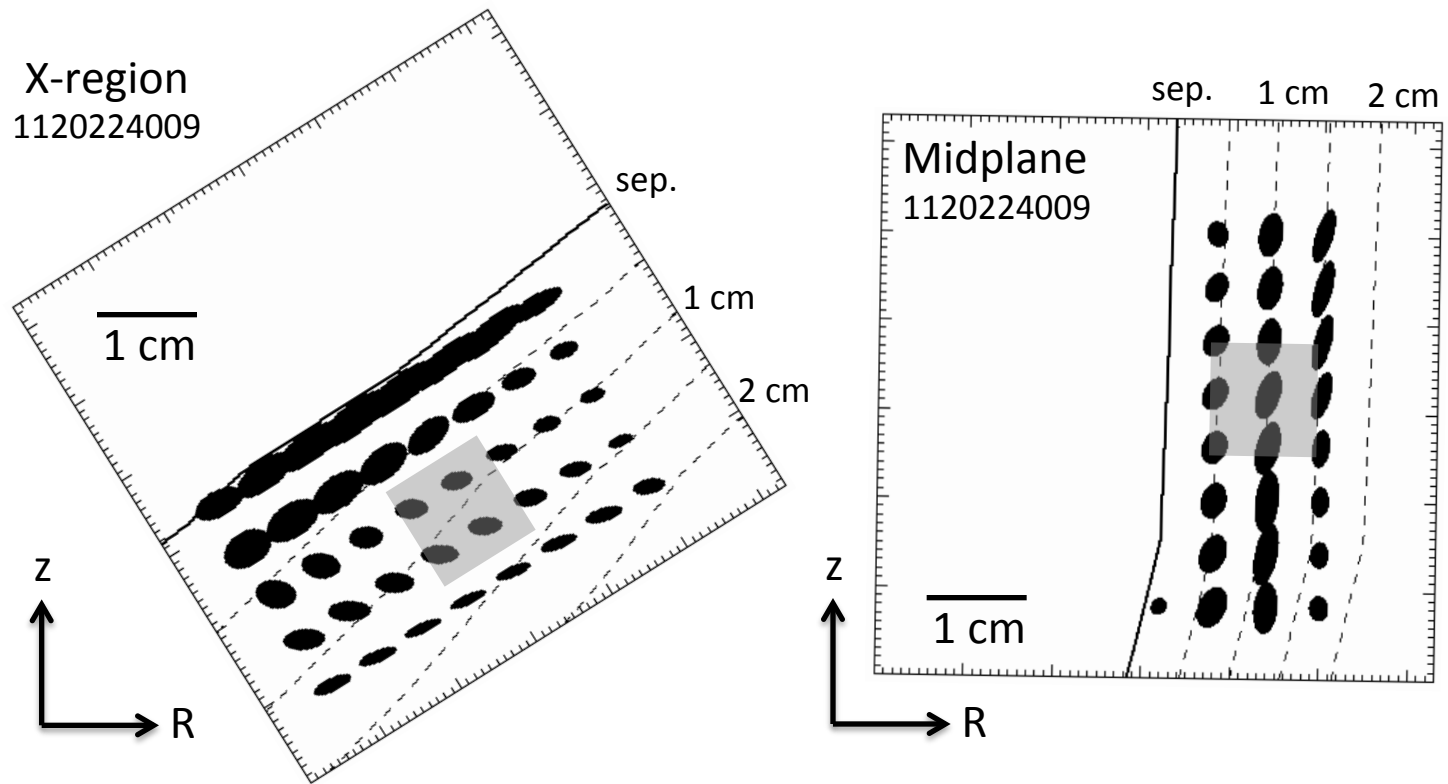


Fig. 5a

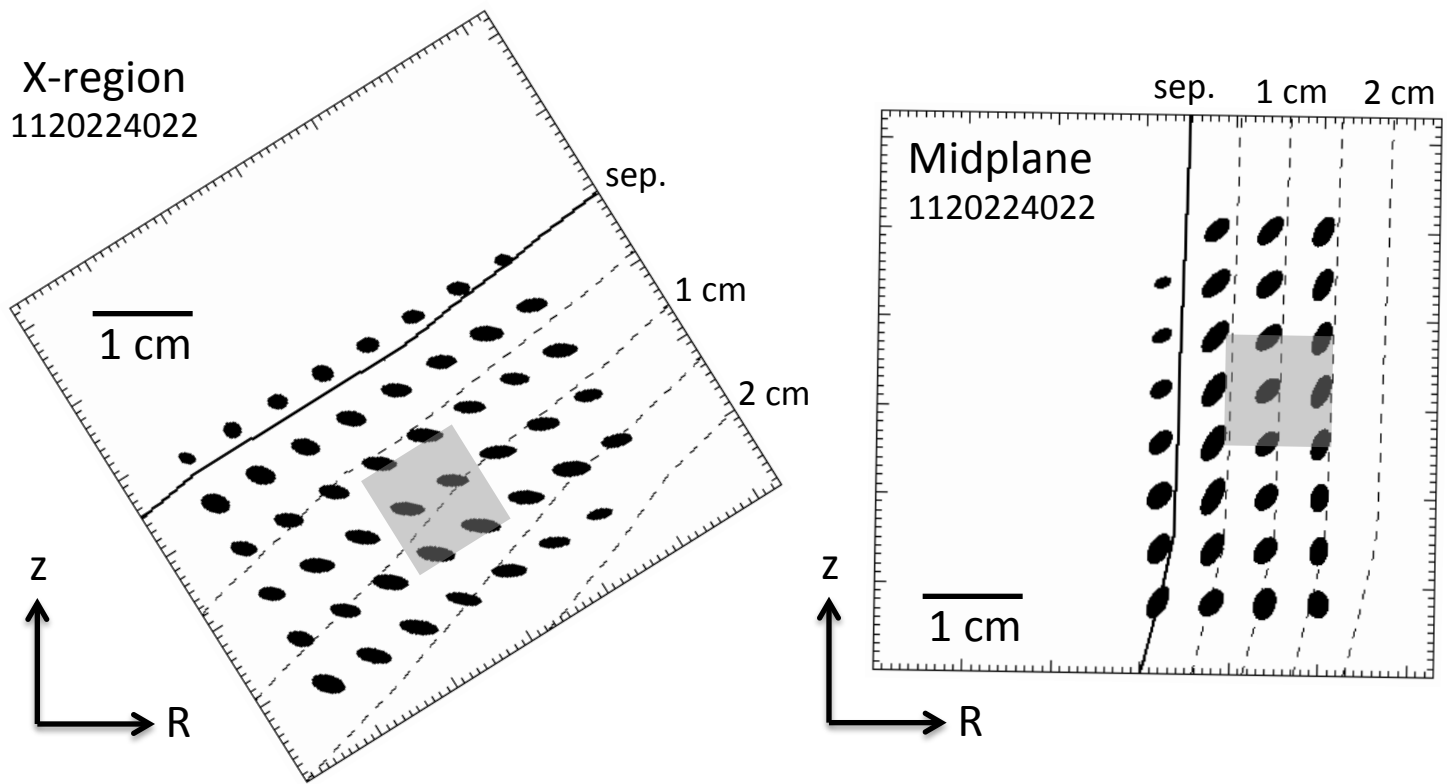


Fig. 5b

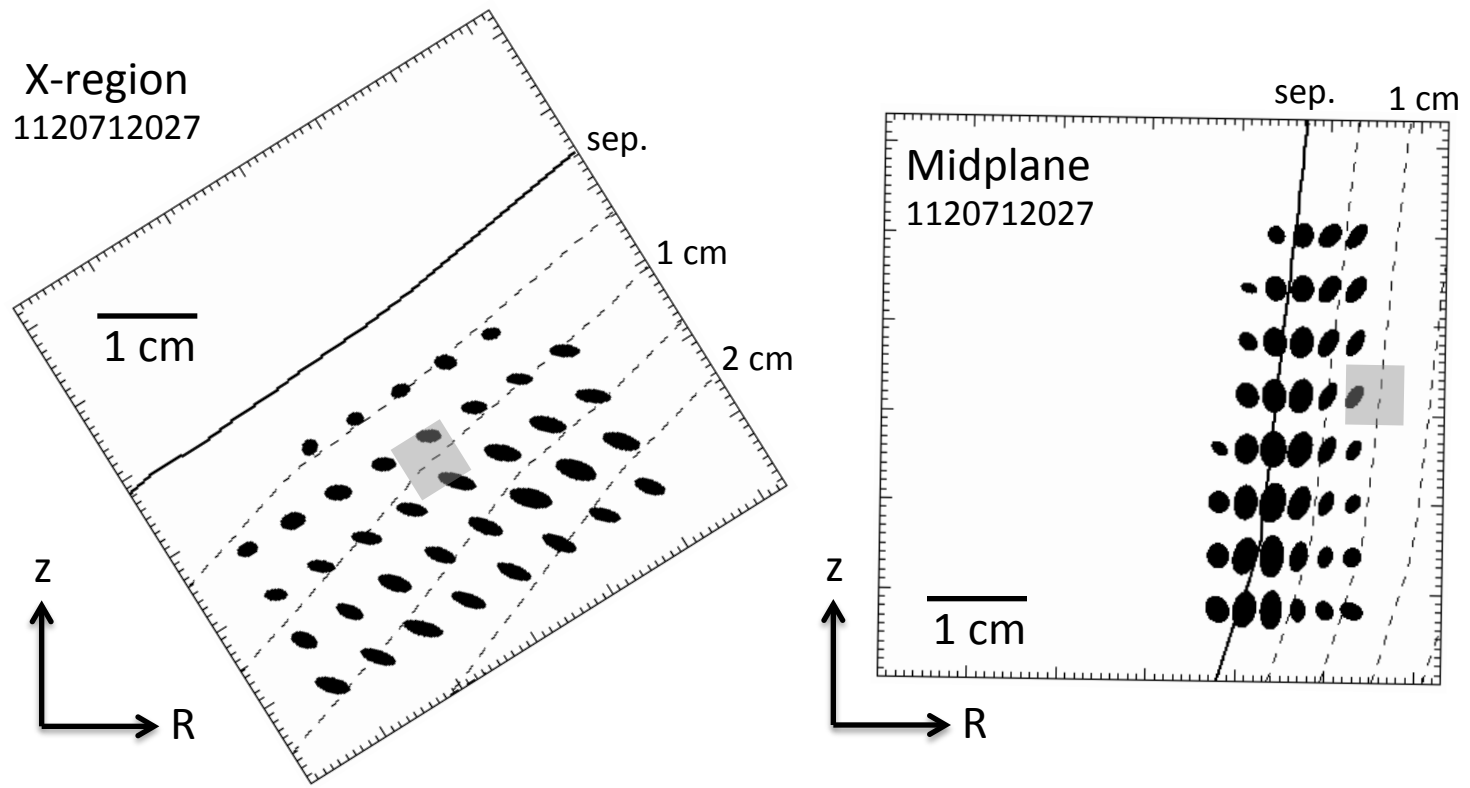


Fig. 5c

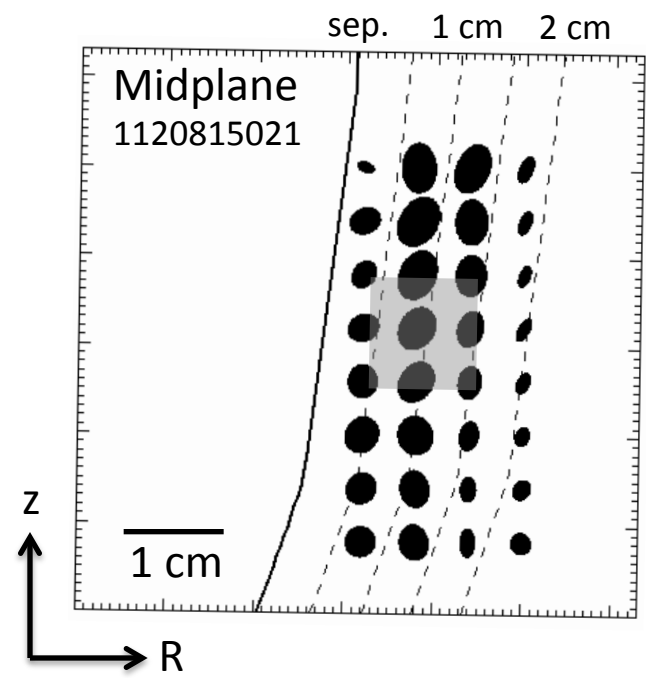
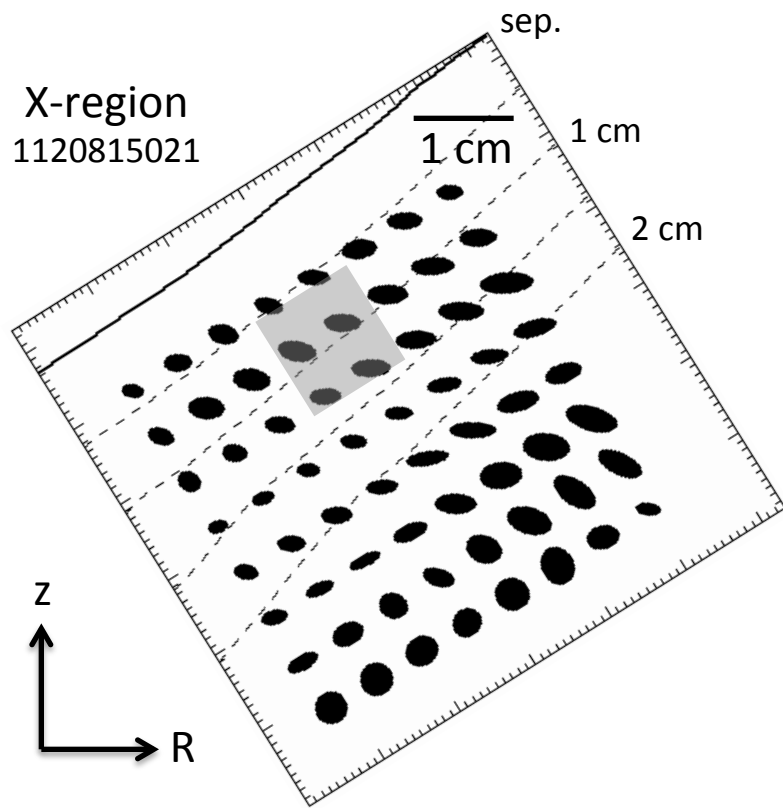


Fig. 5d

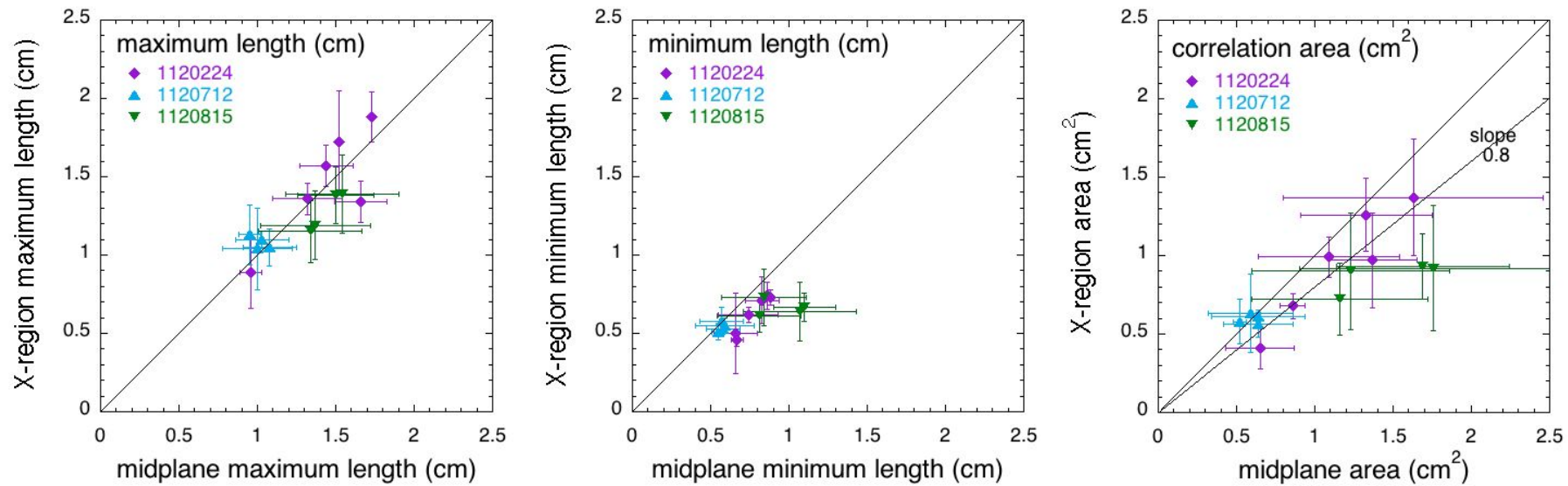


Fig. 6

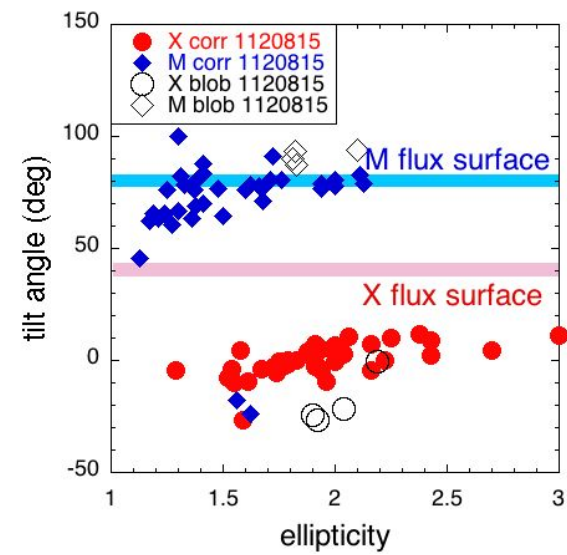
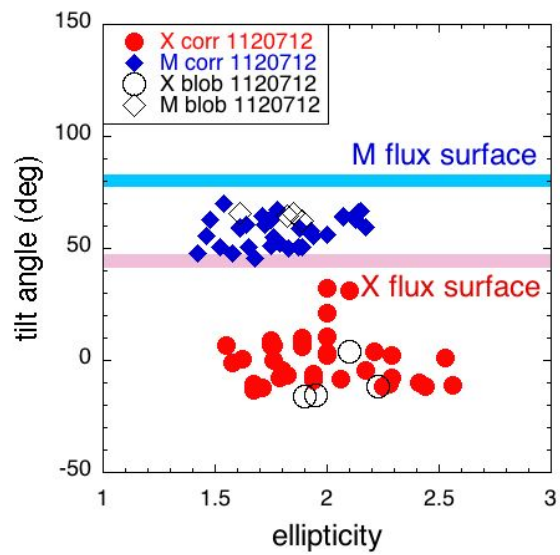
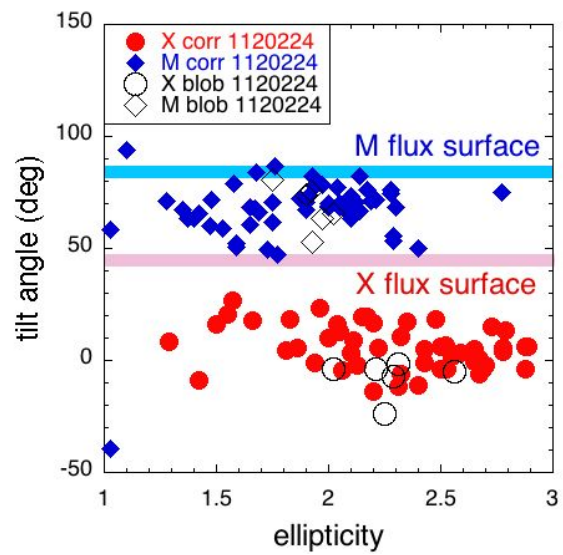


Fig. 7

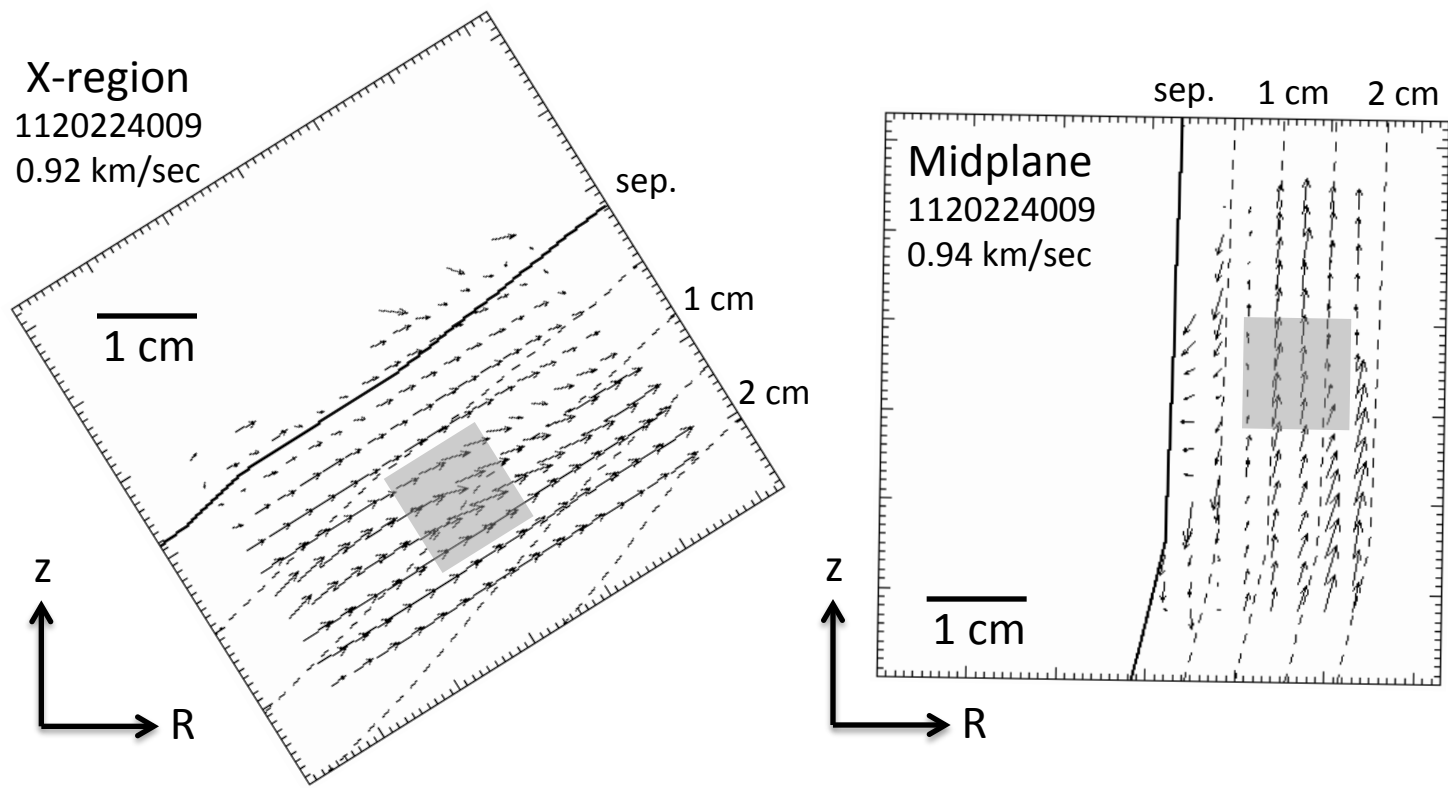


Fig. 8a

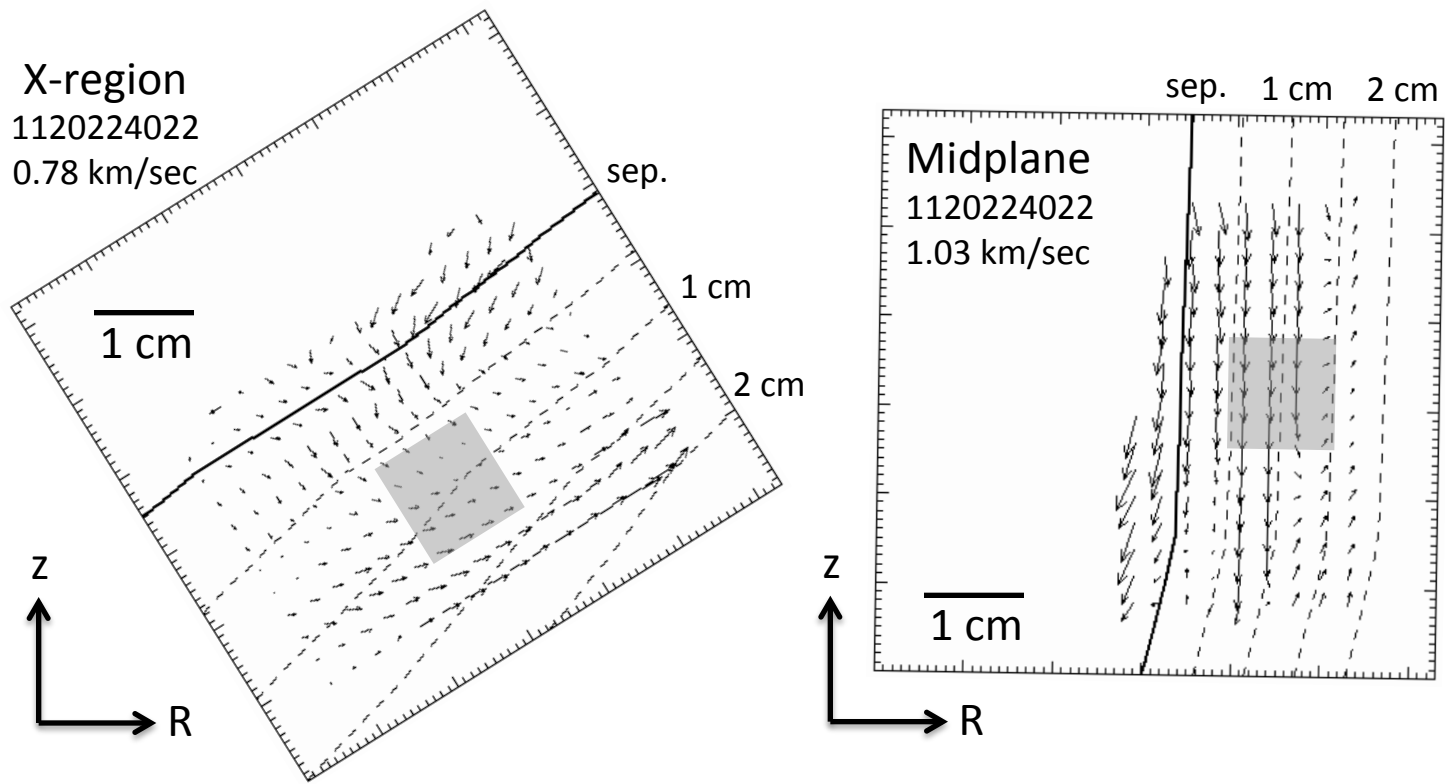


Fig. 8b

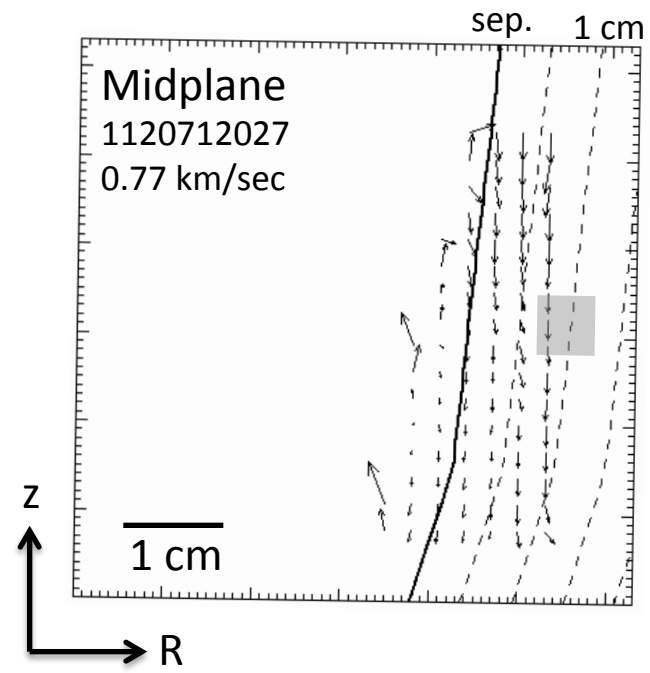
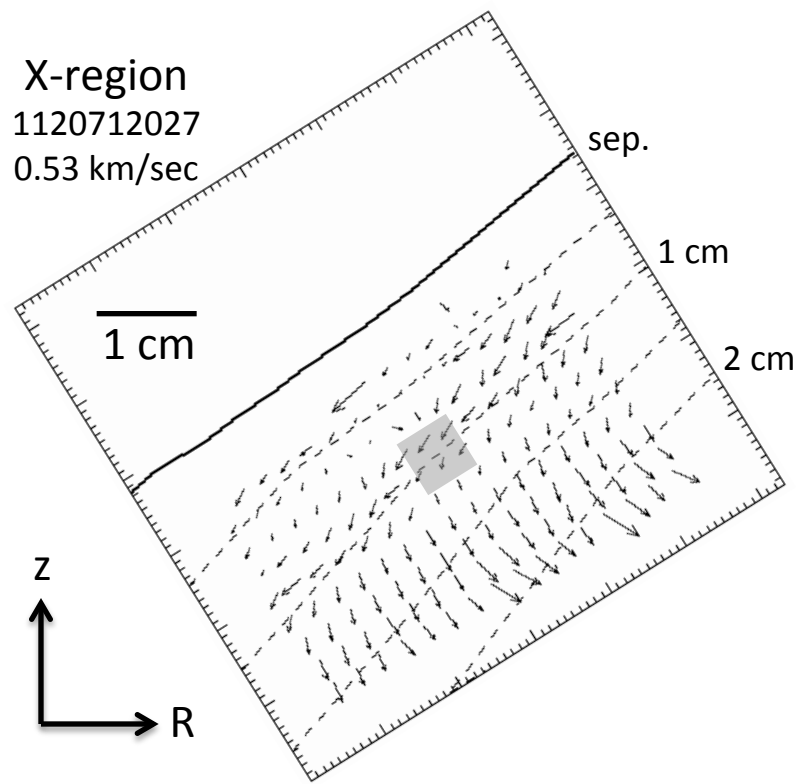


Fig. 8c

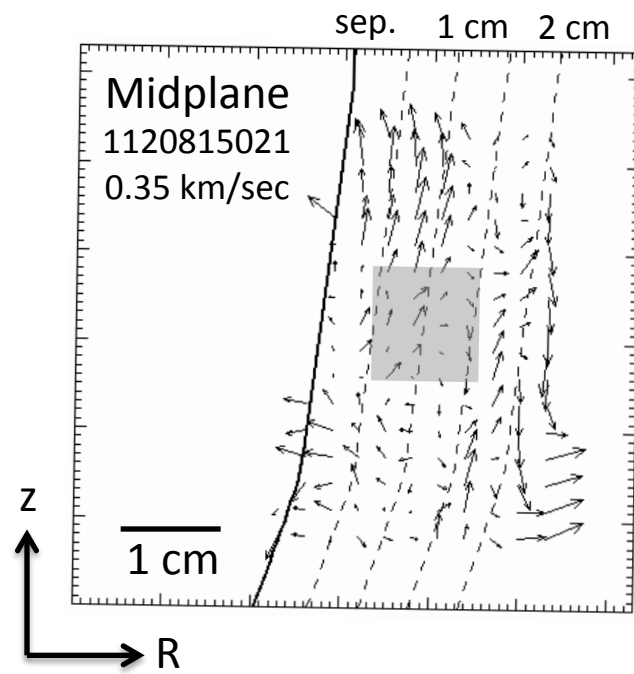
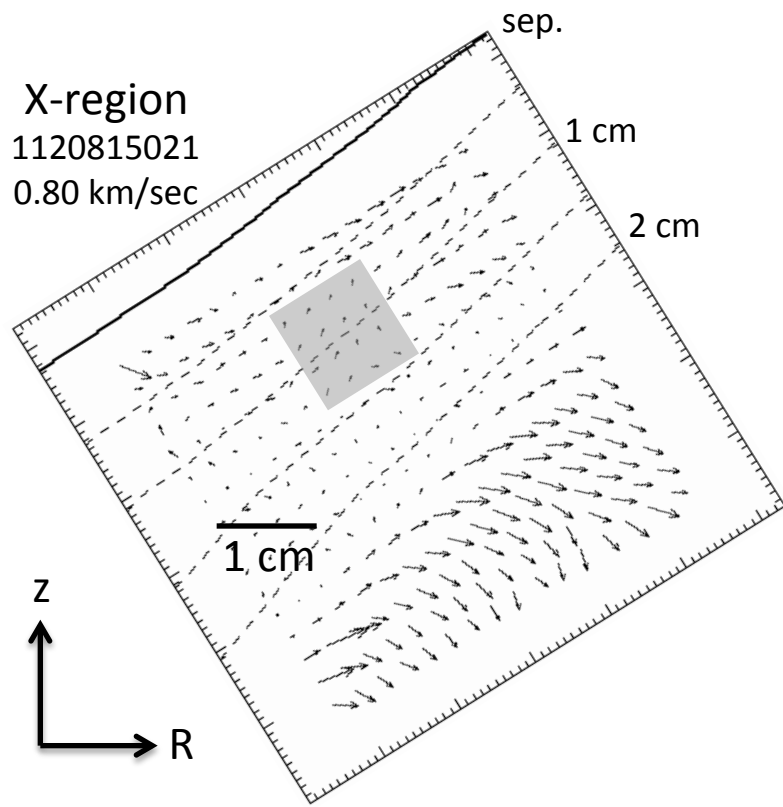


Fig. 8d

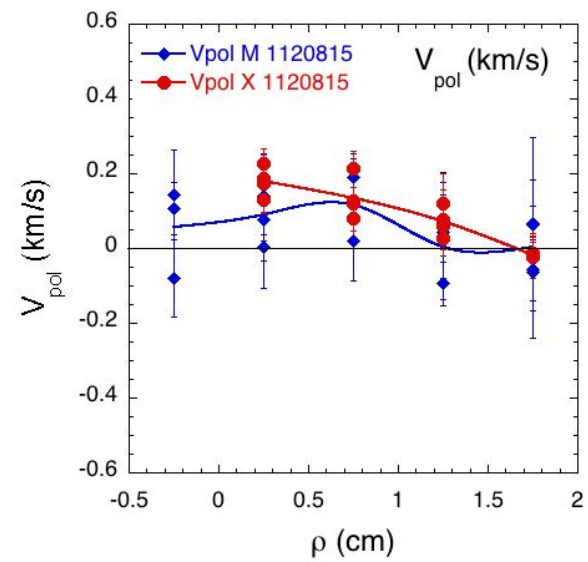
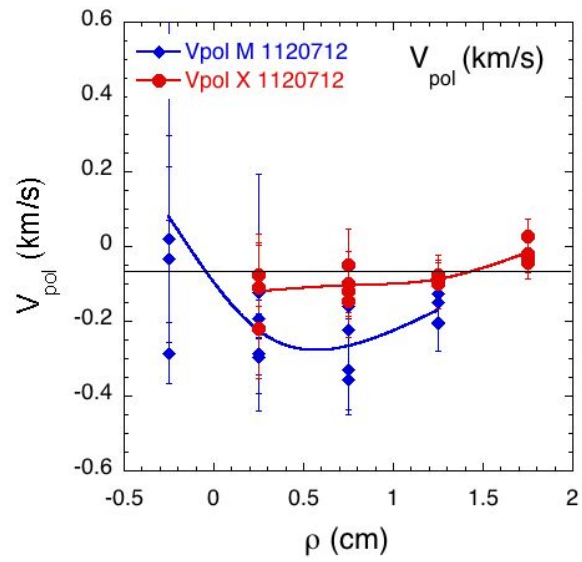
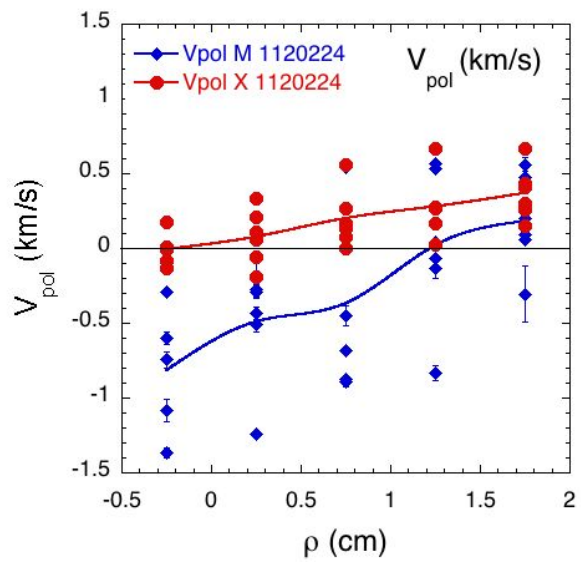


Fig. 9

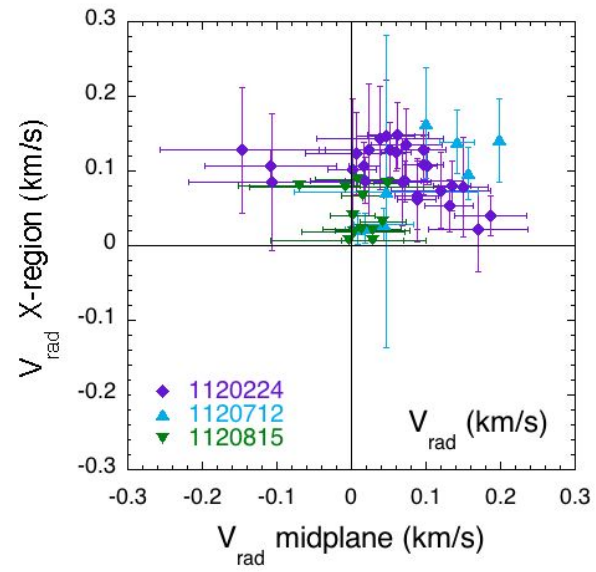
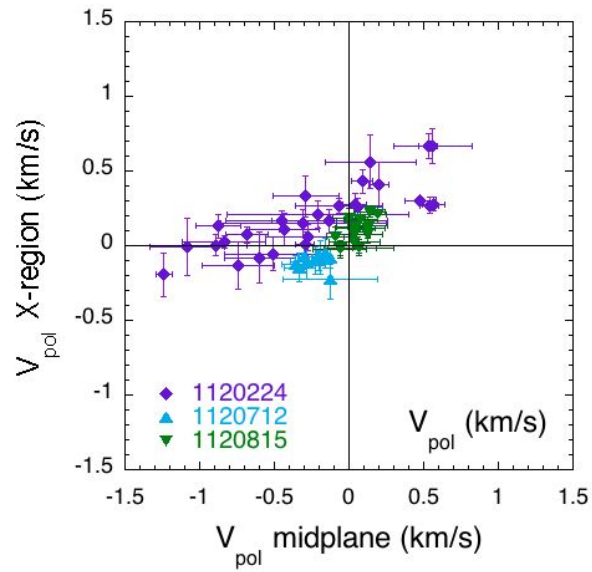


Fig. 10

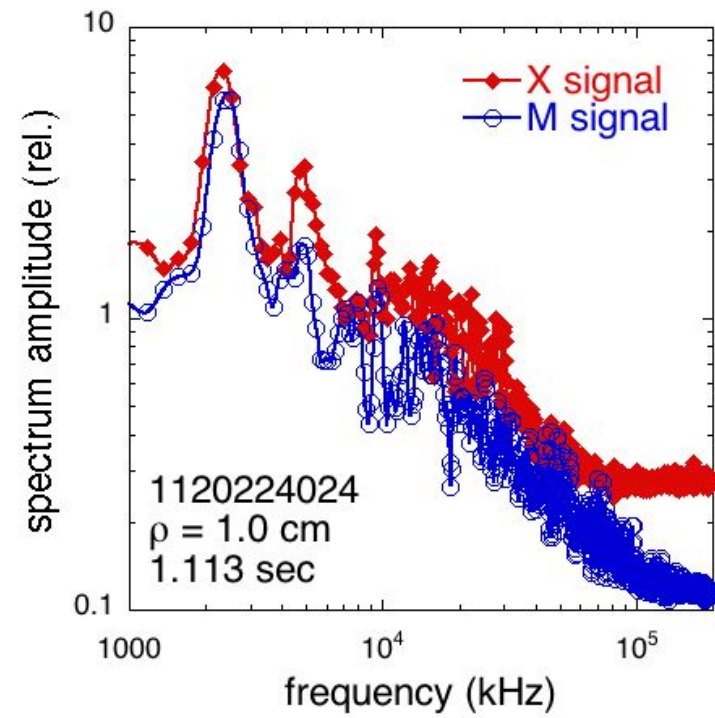
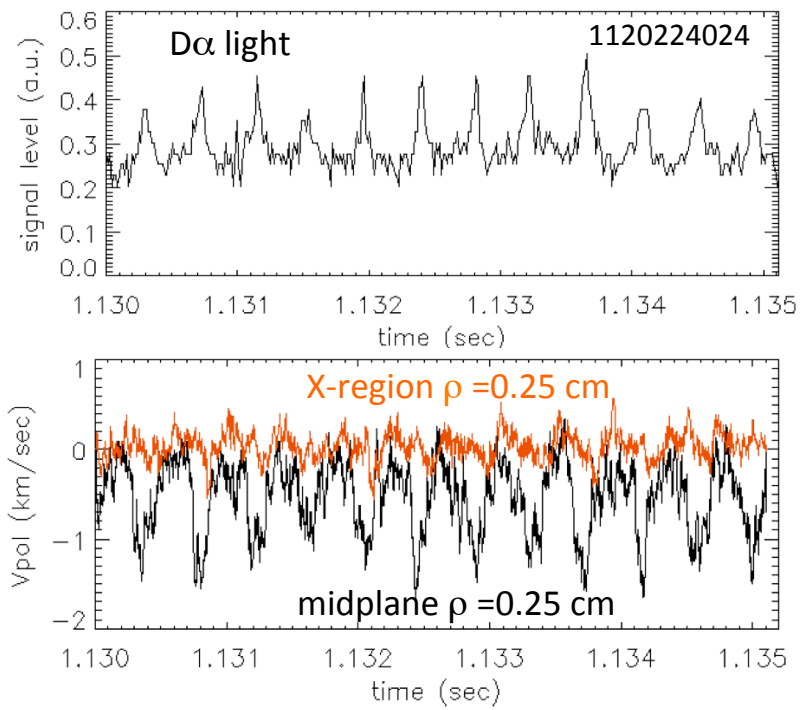


Fig. 11

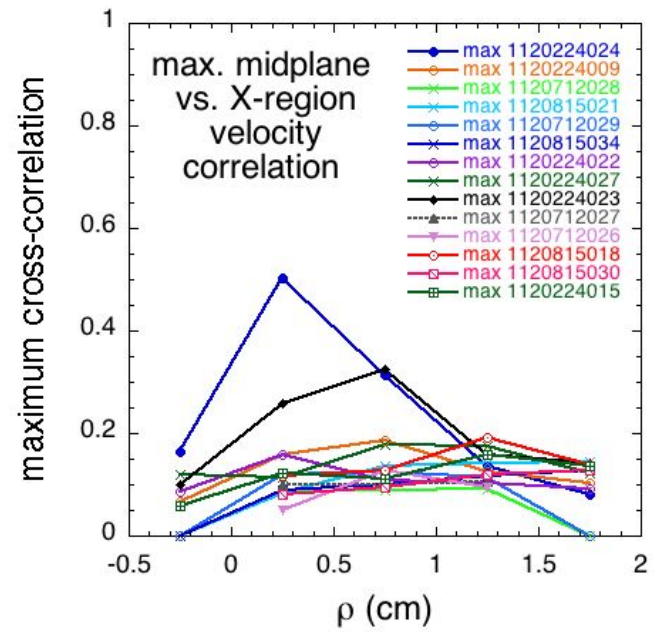


Fig. 12

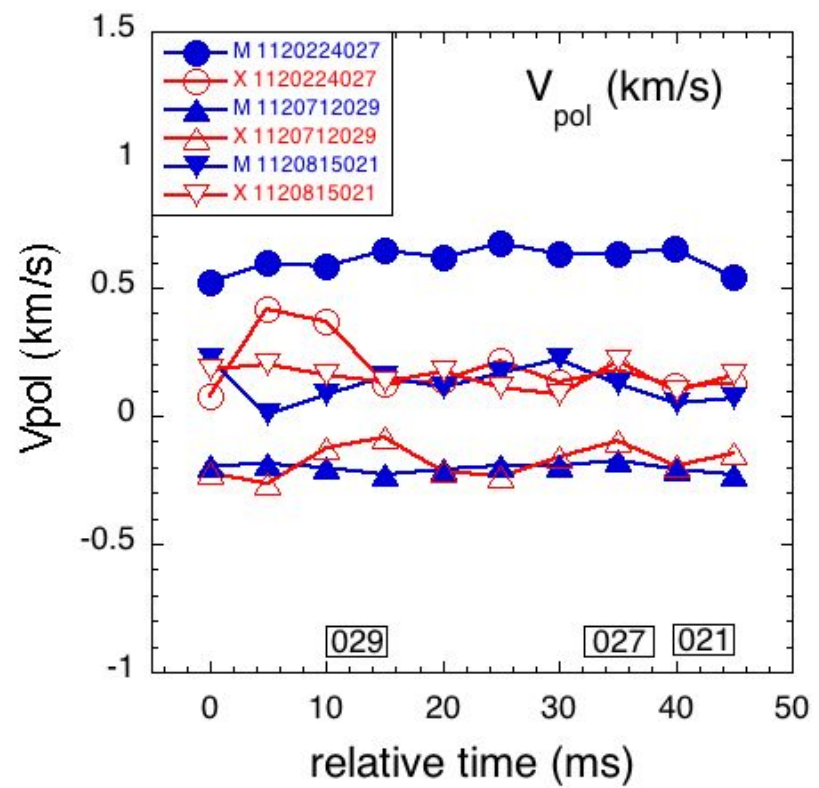
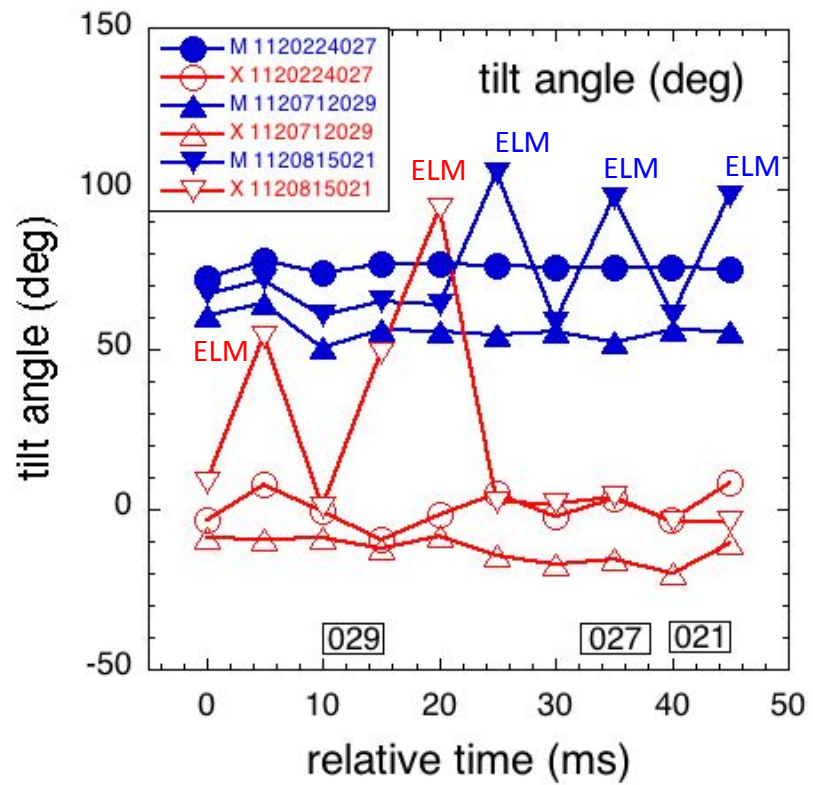


Fig. 13

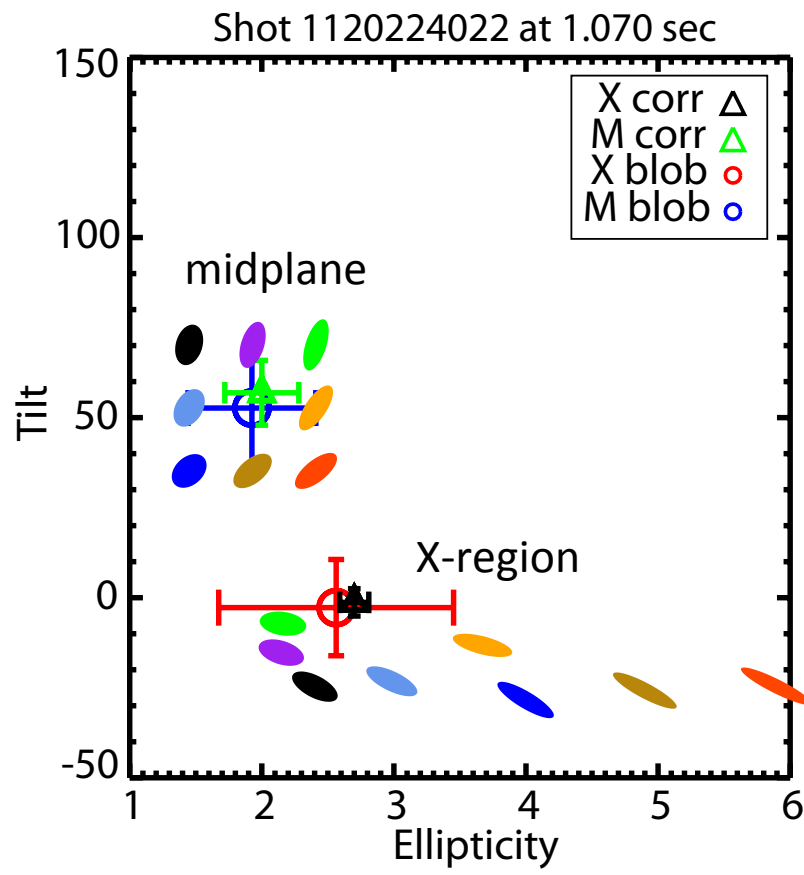


Fig. 14

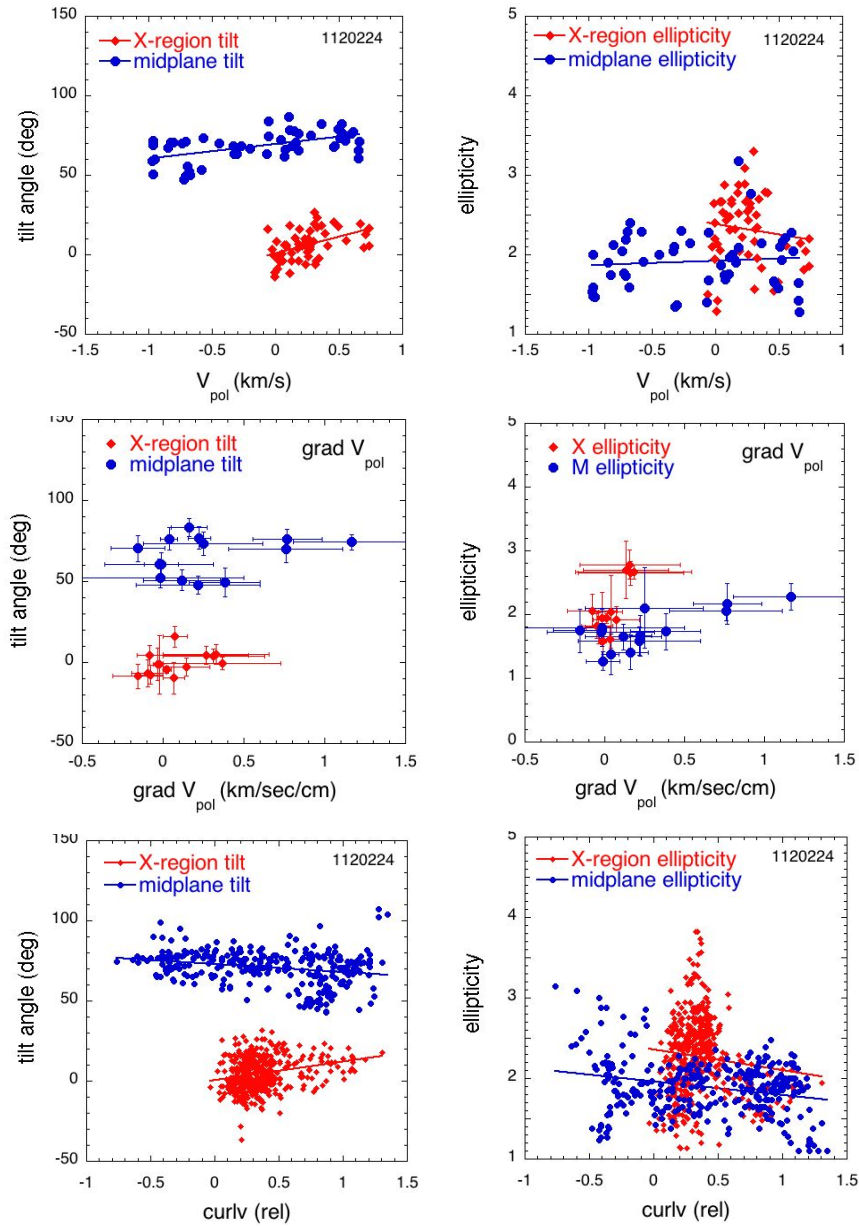


Fig. 15

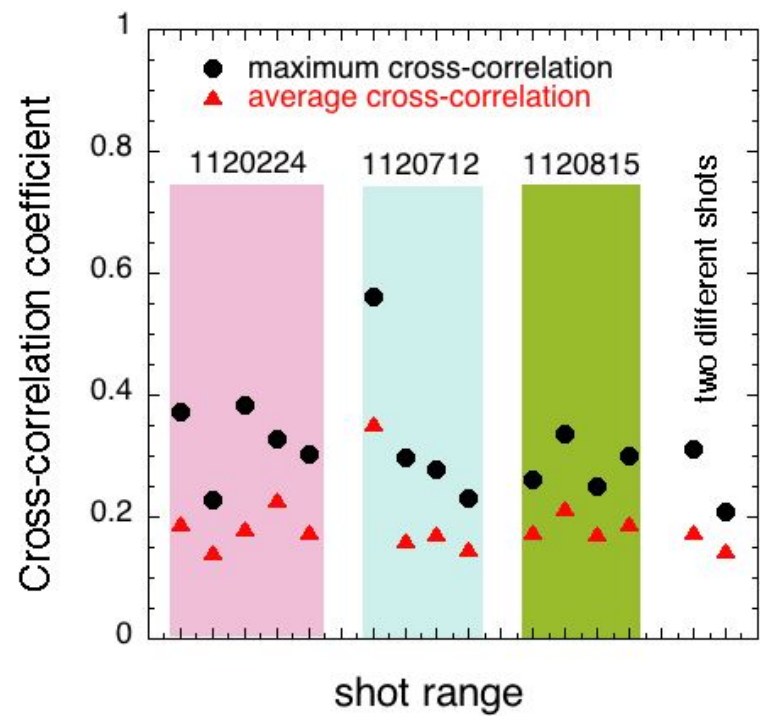
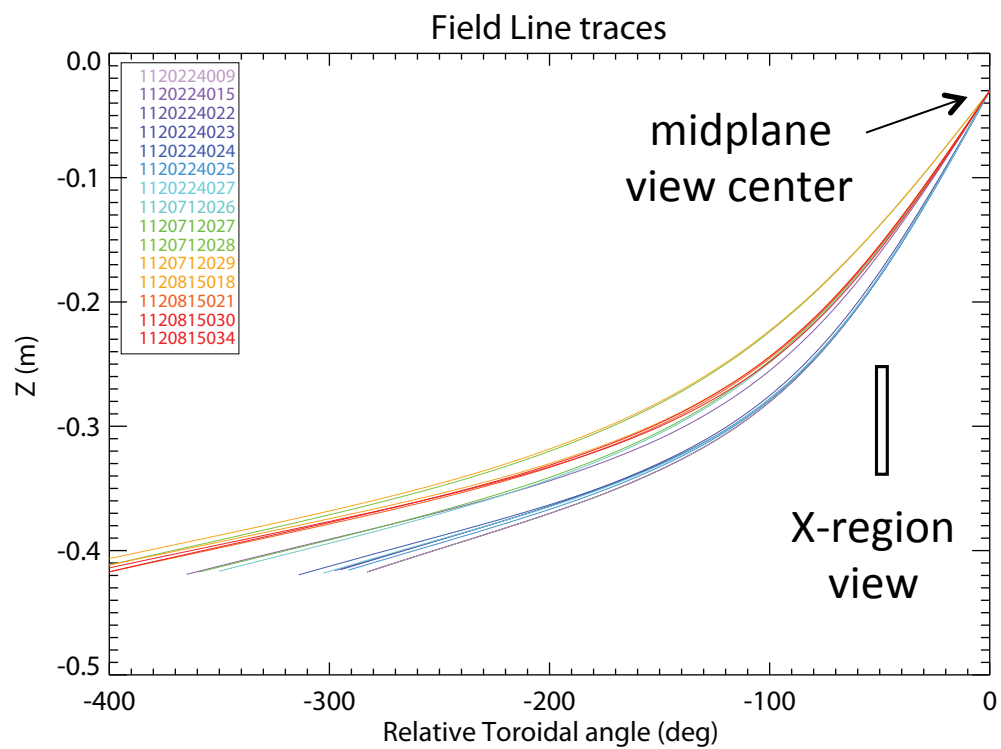


Fig. 16

The Princeton Plasma Physics Laboratory is operated
by Princeton University under contract
with the U.S. Department of Energy.

Information Services
Princeton Plasma Physics Laboratory
P.O. Box 451
Princeton, NJ 08543

Phone: 609-243-2245
Fax: 609-243-2751
e-mail: pppl_info@pppl.gov
Internet Address: <http://www.pppl.gov>